

ISSN: 2349-6495(P) | 2456-1908 (O)



International Journal of Advanced Engineering Research and Science

(IJAERS)

An Open Access Peer-Reviewed International Journal



Journal DOI: 10.22161/ijaers

Issue DOI: 10.22161/ijaers.114

AI PUBLICATIONS

Vol.- 11 | Issue - 4 | Apr 2024

editor.ijaers@gmail.com | editor@ijaers.com | <https://www.ijaers.com/>

International Journal of Advanced Engineering Research and Science (IJAERS)

(ISSN: 2349-6495(P)| 2456-1908(O))

DOI: 10.22161/ijaers

Vol-11, Issue-4

April, 2024

Editor in Chief

Dr. Swapnesh Taterh

Chief Executive Editor

S. Suman Rajest

Copyright © 2024 International Journal of Advanced Engineering Research and Science

Publisher

AI Publication

Email: editor.ijaers@gmail.com; editor@ijaers.com

Web: www.ijaers.com

International Editorial/ Reviewer Board

Editor in Chief

- **Dr. Swapnesh Taterh (Chief-Editor)**, Amity University, Jaipur, India

Chief Executive Editor

- **S. Suman Rajest**, Vels Institute of Science, Technology & Advanced Studies, India
chief-executive-editor@ijaers.com

Associate Editors

- **Dr. Ram Karan Singh**, King Khalid University, Guraiger, Abha 62529, Saudi Arabia
- **Dr. Shuai Li**, University of Cambridge, England, Great Britain

Editorial Member

- **Behrouz Takabi**, PhD, Texas A&M University, Texas, USA
- **Dr. Gamal Abd El-Nasser Ahmed Mohamed Said**, Port Training Institute (PTI), Arab Academy For Science, Technology and Maritime Transport, Egypt
- **Dr. Hou, Cheng-I**, Chung Hua University, Hsinchu Taiwan
- **Dr. Ebrahim Nohani**, Islamic Azad University, Dezful, IRAN.
- **Dr. Ahmadad Nabih Zaki Rashed**, Menoufia University, EGYPT
- **Dr. Rabindra Kayastha**, Kathmandu University, Nepal
- **Dr. Dinh Tran Ngoc Huy**, Banking and Finance, HCM, Viet Nam
- **Dr. Engin NAS**, Duzce University, Turkey
- **Dr. A. Heidari**, California South University (CSU), Irvine, California, USA
- **Dr. Uma Choudhary**, Mody University, Lakshmangarh, India
- **Dr. Varun Gupta**, National Informatic Center, Delhi, India
- **Dr. Ahmed Kadhim Hussein**, University of Babylon, Republic of Iraq
- **Dr. Vibhash Yadav**, Rajkiya Engineering College, Banda. UP, India
- **Dr. M. Kannan**, SCSVMV University, Kanchipuram, Tamil Nadu, India
- **José G. Vargas-Hernández**, University of Guadalajara Periférico Norte 799 Edif. G201-7, Núcleo Universitario Los Belenes, Zapopan, Jalisco, 45100, México
- **Dr. Sambit Kumar Mishra**, Gandhi Institute for Education and Technology, Baniatangi, Bhubaneswar, India
- **DR. C. M. Velu**, Datta Kala Group of Institutions, Pune, India
- **Dr. Deependra Pandey**, Amity University, Uttar Pradesh, India
- **Dr. K Ashok Reddy**, MLR Institute of Technology, Dundigal, Hyderabad, India
- **Dr. S.R.Boselin Prabhu**, SVS College of Engineering, Coimbatore, India
- **N. Balakumar**, Tamilnadu College of Engineering, Karumathampatti, Coimbatore, India
- **R. Poorvadevi**, SCSVMV University, Enathur, Kanchipuram, Tamil Nadu, India
- **Dr. Subha Ganguly**, Arawali Veterinary College, Sikar, India
- **Dr. P. Murali Krishna Prasad**, GVP College of Engineering for Women, Visakhapatnam, Andhra Pradesh, India
- **Anshul Singhal**, Bio Instrumentation Lab, MIT, USA
- **Mr. Lusekelo Kibona**, Ruaha Catholic University, Iringa, Tanzania
- **Sina Mahdavi**, Urmia Graduate Institute, Urmia, Iran
- **Dr. N. S. Mohan**, Manipal Institute of Technology, Manipal, India
- **Dr. Zafer Omer Ozdemir**, University of Health Sciences, Haydarpara, Uskudar, Istanbul, TURKIYE
- **Bingxu Wang**, 2721 Patrick Henry St Apt 510, Auburn Hills, Michigan, United States

- **Dr. Jayashree Patil-Dake**, KPB Hinduja College of Commerce, Mumbai, India
- **Dr. Neel Kamal Purohit**, S.S. Jain Subodh P.G. College, Rambagh, Jaipur, India
- **Mohd Muntjir**, Taif University, Kingdom of Saudi Arabia
- **Xian Ming Meng**, China Automotive Technology & Research Center No.68, East Xianfeng Road, Dongli District, Tianjin, China
- **Herlandi de Souza Andrade**, FATEC Guaratingueta, State Center for Technological Education Paula Souza - CEETEPS
- **Dr. Payal Chadha**, University of Maryland University College Europe, Kuwait
- **Ahmed Moustafa Abd El-hamid Elmahalawy**, Menoufia University, Al Minufya, Egypt
- **Prof. Mark H. Rummeli**, University & Head of the characterisation center, Soochow Institute for Energy Materials Innovations (SIEMES), Suzhou, Jiangsu Province, China
- **Dr. Eman Yaser Daraghmi**, Ptuk, Tulkarm, Palestine
- **Holmes Rajagukguk**, State University of Medan, Lecturer in Sisingamangaraja University North Tapanuli, Indonesia
- **Dr. Menderes KAM**, Dr. Engin PAK Cumayeri Vocational School, DÜZCE UNIVERSITY (University in Turkey), Turkey
- **Dr. Jatin Goyal**, Punjabi University, Patiala, Punjab, India | International Collaborator of GEITEC / UNIR / CNPq, Brazil
- **Ahmet İPEKÇİ**, Dr. Engin PAK Cumayeri Vocational School, DÜZCE UNIVERSITY, Turkey
- **Baarimah Abdullah Omar**, Universiti Malaysia Pahang (UMP), Gambang, 26300, Malaysia
- **Sabri UZUNER**, Dr. Engin PAK Cumayeri Vocational School Cumayeri/Duzce/Turkey
- **Ümit AĞBULUT**, Düzce University, Turkey
- **Dr. Mustafa ÖZKAN**, Trakya University, Edirne/ TURKEY
- **Dr. Indrani Bhattacharyya**, Dr. B.C. Roy College of Pharmacy and Allied Health Sciences, Durgapur, West Bengal, India
- **Egnon Kouakou**, Nutrition/Health at University Felix Houphouet Boigny Abidjan, Ivory Coast
- **Dr. Suat SARIDEMİR**, Düzce University, Faculty of Technology, Turkey
- **Dr. Manvinder Singh Pahwa**, Director, Alumni Relations at Manipal University Jaipur, India
- **Omid Habibzadeh Bigdarvish**, University of Texas at Arlington, Texas, USA
- **Professor Dr. Ho Soon Min**, INTI International University, Jln BBN 12/1, Bandar, Baru Nilai, 71800 Negeri Sembilan, Malaysia
- **Ahmed Mohammed Morsy Hassan**, South Egypt Cancer Institute, Assiut University, Assiut, Egypt
- **Xian Ming Meng (Ph.D)**, China Automotive Technology & Research Center, No.68, East Xianfeng Road, Tianjin, China
- **Ömer Erkan**, Konuralp Campus, Düzce-Turkey
- **Dr. Yousef Daradkeh**, Prince Sattam bin Abdulaziz University) PSAU), KSA
- **Peter JO**, IPB University, Indonesia
- **Nazmi Liana Binti Azmi**, Raja Perempuan Zainab II Hospital, 15586 Kota Bharu, Kelantan, Malaysia
- **Mr. Sagar Jamle**, Oriental University, Indore, India
- **Professor Grazione de Souza**, Applied Mathematics, Rio de Janeiro State University, Brazil
- **Kim Edward S. Santos**, Nueva Ecija University of Science and Technology, Philippines.

Vol-11, Issue-4, April, 2024

(10.22161/ijaers.114)

Detail with DOI (CrossRef)

Utilization of Form-Stable Paraffin/Nano-Silica Phase Change Materials for Thermal Energy Storage Enhancement in Mortar

Md. Rasidul Islam, Xiangyu Li

 DOI: [10.22161/ijaers.114.11](https://doi.org/10.22161/ijaers.114.11)

Page No: 01-09

Numerical Study of Casson Nanofluid Flow over a Stretching Surface

Usama, Muhammad Amad Sarwar, Muhammad Awais, Muhammad Mukhtar Khan, Ioannis Sarris

 DOI: [10.22161/ijaers.114.12](https://doi.org/10.22161/ijaers.114.12)

Page No: 10-23

Reuse of Greywater and its Role in the Sustainability of Water Resources – A Study in Saudi Arabia

Anbarah Khamis B. Al-Saud

 DOI: [10.22161/ijaers.114.13](https://doi.org/10.22161/ijaers.114.13)

Page No: 24-29

Design and Simulation of InGaAs/GaAsSb single quantum well structure for optical fiber application: Electronic Band Structure, Carrier Transport, and Optical Gain Analysis

Jayprakash Vijay

 DOI: [10.22161/ijaers.114.14](https://doi.org/10.22161/ijaers.114.14)

Page No: 30-33

Fe₃O₄.CeO₂/SiO₂ oxide nanocomposite as a Fenton-like catalyst for degradation of Congo red

Nguyen Manh Ha, Bui Thi Hai Yen, Vu Ngoc Hai, Tran Ngoc Hieu, Nguyen Thi Phuong

 DOI: [10.22161/ijaers.114.15](https://doi.org/10.22161/ijaers.114.15)

Page No: 34-39

Utilization of Form-Stable Paraffin/Nano-Silica Phase Change Materials for Thermal Energy Storage Enhancement in Mortar

Md. Rasidul Islam, Xiangyu Li*

Department of Civil Engineering, Taiyuan University of Technology -TYUT, Shanxi, China

Received: 11 Feb 2024,

Receive in revised form: 20 Mar 2024,

Accepted: 03 Apr 2024,

Available online: 10 Apr 2024

©2024 The Author(s). Published by AI
Publication. This is an open access article
under the CC BY license

[\(https://creativecommons.org/licenses/by/4.0/\)](https://creativecommons.org/licenses/by/4.0/)

Keywords— Cement-Based Materials,
Paraffin, Silica, Thermal Conductivity,
Thermal Control Effect Test.

Abstract— This research explores the utilization of form-stable paraffin/nano-silica phase change materials (PCMs) to improve thermal energy storage in mortar. The composite PCM, comprising paraffin enclosed within a nano-silica framework, offers enhanced stability and compatibility with mortar compared to traditional PCM systems. Experimental investigations were conducted to assess the thermal performance and mechanical properties of mortar specimens incorporating varying concentrations of form-stable PCM. Thermal conductivity, heat storage capacity, and mechanical strength were analysed through thermal cycling tests and mechanical testing methods to understand the impact of PCM content. Results demonstrate that integrating form-stable paraffin and nano-silica PCMs enhances thermal energy storage capabilities in mortar while minimally affecting mechanical strength. Moreover, the nano-silica matrix facilitates better dispersion and adhesion of paraffin particles within the mortar matrix, addressing concerns related to PCM leakage and separation during hydration. This study underscores the viability and efficacy of employing form-stable paraffin and nano-silica PCMs to enhance thermal energy storage in mortar, offering a promising avenue for sustainable and energy-efficient construction materials.

I. INTRODUCTION

Paraffin hydrocarbons are saturated hydrocarbons with the formula C_nH_{2n+2} , where 'n' represents an integer, 'C' stands for carbon, and 'H' stands for hydrogen. Incorporating phase change materials (PCM) into building materials offers numerous benefits. PCM integration enhances energy storage in walls, ceilings, and floors, thereby improving a building's thermal performance. Additionally, PCM can increase thermal inertia and indoor thermal stability, promote the use of renewable energy sources, facilitate passive cooling strategies, and offer various other advantages [1,2, 3]. PCM materials come in diverse compositions and properties, typically classified as organic, inorganic, and eutectic materials [4,5,6]. Various

methods [7], including direct application, are employed for integrating PCM into building materials.

This study focuses on the mechanical and physical behaviour of protected phase change material (PCM) incorporated into Portland cement mortars. The PCM consists of dry dust microparticles conforming to a silica-based matrix with a poly-nucleus of paraffin. Portland cement mortars were selected for this investigation due to their ability to accommodate paraffin particles and effectively interact with the silica matrix. This particular type of PCM offers several advantages for mortar applications. It enhances the mortar's heat storage capacity, reduces retraction, and mitigates issues related to thermal conductivity, thereby making it well-suited for thermal applications. However, a significant drawback of this PCM

is the potential for PCM leakage when employing direct methods for its incorporation into mortar mixtures. This leakage issue has been identified as a primary reason for the limited research studies on this type of PCM integration [8].

Numerous research studies have explored the incorporation of phase change materials (PCM) into mortar and concrete mixtures using various methods such as direct mixing, immersion, and impregnation in porous aggregates [9]. Here are some examples: PCM impregnation in light sands [10], PCM impregnation in concrete blocks [11], and the utilization of burnt clay aggregate to enhance the thermal properties of concrete panels [12]. Investigation into the impact of light sand impregnated with PCM on the thermal behaviour of concrete during setting and freeze conditions [13] has also been conducted. Moreover, significant advancements have been made in PCM technology, leading to the development of innovative materials like cement-based composite phase change materials (CCPCMs). These materials leverage the hydraulic properties of cement and the water solubility of substances like polyethylene glycol (PEG) [14] to enhance thermal performance. Additionally, PCM coatings have been developed, such as salt hydrate/diatomite PCM coated with polyurethane acrylate, which exhibit improved thermal stability [15].

The thermal properties of cement-based materials modified with phase change materials (PCM) for building construction have been extensively investigated both experimentally and numerically, as highlighted in a study [16]. Additionally, a recent review [17] has examined the potential of microencapsulated PCM for energy savings in buildings. Studies on the application of PCM, particularly those based on paraffin nuclei and polymeric shells, to Portland cement mortars have revealed significant changes in the mixtures. These changes include a decrease in resistance. The incorporation of PCM into cement mortars has been associated with a decrease in mechanical strength or resistance and an increase in water content. PCM addition often leads to an increase in the water content of cement mortars and a decrease in thermal conductivity. PCM-modified mortars typically exhibit lower thermal conductivity, which contributes to improved thermal insulation properties and an increase in heat capacity. The presence of PCM in cement mortars enhances their heat storage capacity, enabling them to absorb and release heat more effectively [18,19, 20,21]. The study conducted by Cunha et al. [22] focused on the direct addition of phase change material (PCM) particles to mortars, demonstrating that mortar mixtures exhibit favourable physical and mechanical characteristics. Similar positive outcomes have been observed when PCM is combined with other

substances such as silica [23,24], graphite [25], or diatomite [26,27]. Furthermore, investigations have explored the impact of microencapsulated phase change materials (MPCM) on Portland cement concretes (PCC) and their microstructure [28]. The results revealed that increasing the amount of MPCM led to a decrease in the compressive strength of PCC. Recently, forest biomass ashes (FBA) have been studied in cement-based mortars [29]. The findings indicated a slight reduction in mechanical strength but an increase in ductility. Additionally, it has been suggested that the use of these mortars is not hindered by the addition of FBA waste.

This study distinguishes between two types of phase change materials (PCM) that may be incorporated into Portland cement mortars: protected PCM and non-protected PCM. Protected PCM, characterized by a stable shell [30], is created using a silica-based matrix with poly-nuclei of paraffin from dry dust microparticles. However, a significant drawback of protected PCM is the potential for microparticle leakage during mixing due to the separation of silica and paraffin upon contact with water. Some authors [31] have proposed solutions to this issue by modifying PCM using different types of nano silica. On the other hand, non-protected PCM lacks such a protective shell. Despite the risk of filtration during mixing or application to porous materials, non-protected PCM offers advantages such as higher heat-storage capacity compared to inorganic PCM, attributable to the absence of a shell [32]. Furthermore, direct incorporation of non-encapsulated PCM avoids the need for complicated incorporation techniques, leading to cost reduction. Consequently, direct incorporation of non-encapsulated PCM represents an innovative and promising approach to significantly enhancing the energy efficiency of buildings [33–34].

In this study, various mixtures were developed with different Phase Change Material (PCM) contents, water-to-cement ratios (w/c), and two types of cement to analyse the impact of PCM addition to Portland cement mortars. Key properties such as apparent density, water absorption, open porosity, compressive strength, air content, and behaviour analysis after exposure to 35°C were investigated. The inclusion of compressive strengths, types of cement, water/cement ratios, and air content in the study provides valuable insights directly applicable to the mixing design process for Portland cement mortars. A notable aspect of the study was the implementation of cooling methods during the mixing process to prevent paraffin leaks. This approach differs from previous studies and ensures that the integrity of the PCM is maintained throughout the mixing process, thereby avoiding potential issues related to PCM leakage.

II. MATERIALS

Raw Materials:

In the study, Portland cement PO 42.5 produced by Taiyuan Co. Ltd., in accordance with relevant Chinese standards, was utilized. The polycarboxylate superplasticizer, with a solid content of 20%, was custom-made by the manufacturer for the experiments. Standard sand meeting the Chinese ISO sand standard GB/T17671 was sourced from Xiamen Aisio Standard Sand Co. Ltd. Tap water served as the primary solvent for the experimental procedures.



Fig.1: Photograph of paraffin.

III. EXPERIMENT

Cement mortar workability test and mix ratio selection:

A workability test was conducted following the guidelines outlined in GB/T2419-2005. The test employed a vibrating table to assess the consistency and workability of the newly formulated mortar. The content of polycarboxylate superplasticizer in the cement mortar was determined through this fluidity test, which provided insights into the mortar's flow characteristics and the effectiveness of the superplasticizer in enhancing workability.

Preparation of cement mortar samples:

Cement mortar samples containing varying amounts of paraffin (**Fig. 1**) were prepared according to the mixing proportions outlined in **Table 1**. The water-to-cement ratio was maintained at 0.4, and the cement-to-sand ratio was kept at 1:2 across all samples. To ensure consistent fluidity for each cement mortar sample, the dosage of the water reducer was adjusted proportionally with the increase in paraffin dosage. Sample M represents plain cement mortar without the addition of paraffin.

The cement mortar was prepared as follows:

1. A mixing pot was utilized, into which the paraffin-mixed solution and cement were added. The pot was then positioned on a fixed frame, and the mixture was stirred at

low speed for 30 seconds. Following the initial 30 seconds of mixing, standard sand was evenly introduced into the mixing pot via a mixing funnel. Subsequently, the mixture was stirred at a high speed for an additional 30 seconds.

2. After the mixing process ceased, any material adhering to the sides of the mixing bowl was promptly scraped down into the batch. The mixer enclosure was then closed, or alternatively, the bowl was covered with a lid. The paste was allowed to stand undisturbed for a duration of 90 seconds.

3. Following the resting period, the mixture underwent further mixing for 60 seconds at high speed.

4. The freshly prepared cement mortar was poured into steel molds and compacted using a standard vibrating table. The molds were subsequently sealed with polyethylene nanosheets to prevent moisture loss. After a curing period of 24 hours, the samples were demolded and subjected to further curing in a saturated lime-water bath maintained at 20°C for specific aging durations of 3, 7, and 28 days.

Table-1: Mixing proportions of paraffin/silica cement mortar samples

Cement(g)	Sand(g)	Water(g)	Paraffin(g)	SiO ₂ (g)	PC(g)
468	1200	240	120	12	5
501	1200	240	90	9	4
435	1200	240	150	15	6.5
402	1200	240	180	18	8.5

IV. MECHANICAL TEST

A steel mold measuring 40mm × 40mm × 160mm was chosen for the flexural and compressive strength tests. The flexural and compressive strengths of the specimens were assessed in accordance with the guidelines outlined in GB/T17671-1999 at three different aging durations: 3, 7, and 28 days. For each series, three specimens were subjected to testing to determine their strength characteristics. The flexural strength test was conducted utilizing a three-point bending test apparatus with a loading rate of 0.06 N/s. This test method provides insights into the ability of the specimens to resist bending forces. On the other hand, the compressive strength test involved subjecting the specimens to compression using a loading rate of 2.4 kN/s. This test evaluates the ability of the specimens to withstand compressive forces.

SEM characterization of hydration products:

In this study, the scanning electron microscope (SEM) model ZEISS Gemini SEM 300 was employed to directly

observe the microscopic morphology of the materials by imaging the surface properties of the sample. The working principle of SEM involves using an electron lens to reduce a single electron beam spot to a nanoscale size. Subsequently, a deflection system is utilized to raster scan the high-energy electron beam across the surface of the sample, exciting secondary electrons and other physical information. These signals are collected by detectors and converted into an image for display. The SEM equipment used in this study offers a scanning speed ranging from 20 nanoseconds to 10 milliseconds per pixel and a magnification capability ranging from 1 to 1 million times. Figure 2 depicts the SEM equipment utilized.

Furthermore, it is imperative that the samples for SEM testing are dry. Therefore, prior to SEM observation, cement hydration suspension treatment is necessary due to the continuous hydration process of cement. Suspension of hydration and drying can be carried out simultaneously. In this experiment, a combination of solvent substitution and vacuum drying was employed. Solvent substitution involves using organic solvents to displace water from the sample. Specifically, the samples were soaked in absolute ethanol for 24 hours. Subsequently, the samples were placed in a vacuum drying oven set at 60°C for 6 hours to facilitate the volatilization of absolute ethanol from the samples.



Fig.2: Photograph of Scanning electron microscope (SEM)

V. RESULT AND DISCUSSION

Effects of the paraffin on the workability of cement paste:

The fluidity (Fig. 3) of cement mortar decreases as the phase-change materials (PCMs)/paraffin content increase. Specifically, compared to cement mortar M, the fluidity decreases by 10.9% when the phase-change materials (PCMs)/paraffin content is 15% and by 18.48% when the phase-change materials (PCMs)/paraffin content

is 20%. This reduction in fluidity is likely due to the distribution and orientation of the phase-change materials (PCMs)/paraffin materials within the mortar. To ensure consistency in fluidity values and enable the comparison of strengths, a water-reducing agent was added to the samples. This addition helps maintain consistent fluidity across the samples, facilitating an accurate comparison of their strengths. Figure 3 illustrates the observed trends in fluidity as the phase-change materials (PCMs)/paraffin content vary, providing a visual representation of the relationship between phase-change materials (PCMs)/paraffin content and fluidity in cement mortar samples.

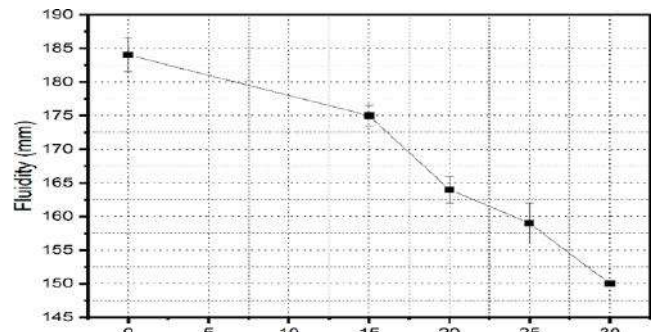


Fig.3: Workability test compared to Ordinary mortar and paraffin composite

Flexural Strength

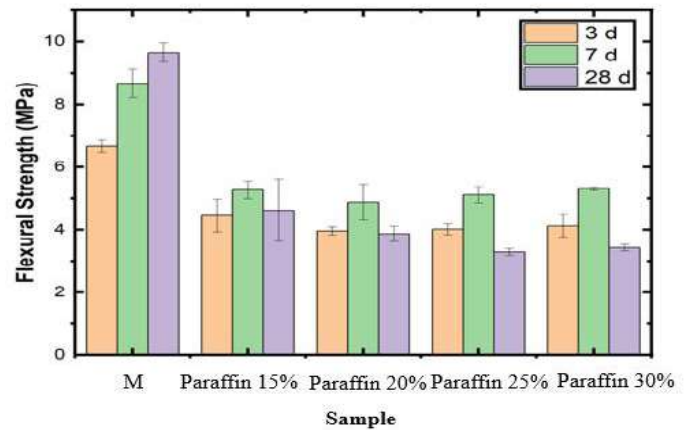


Fig.4: Photograph of Flexural Strength

Figure 4 illustrates the flexural strength of cement mortar mixed with varying amounts of paraffin at 3, 7, and 28 days. Initially, the flexural strength of the cement mortar increases gradually with an increase in the paraffin content. However, beyond an optimal paraffin content, the flexural strength begins to decrease. The flexural strength of the cement mortar mixed with paraffin is highest when the paraffin content is 15%, 20%, 25%, or 30%. At curing ages of 3 days and 7 days, the flexural strength of sample

paraffin increases by 5%, 4.5%, 5.2%, and 5.5%, respectively, compared to that of plain cement mortar sample M. This increase in flexural strength is attributed to the high strength of paraffin, which enhances the mechanical properties of the cement mortar.

Compressive Strength

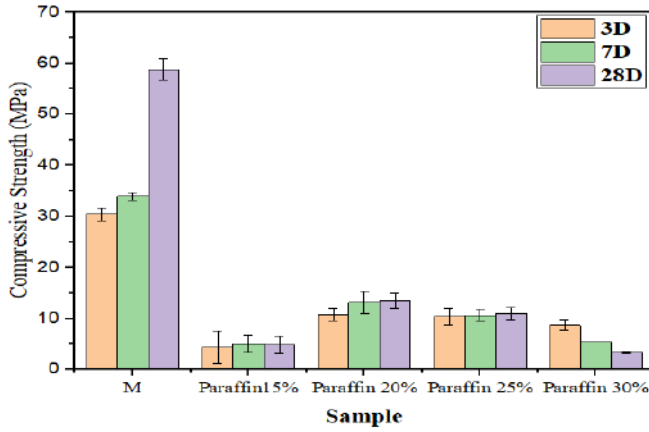


Fig.5: Photograph of Compressive Strength

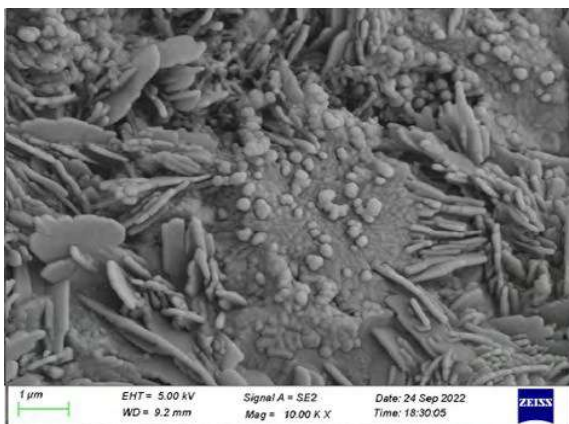
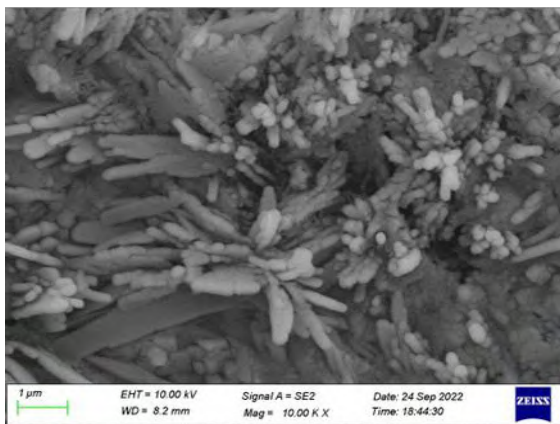
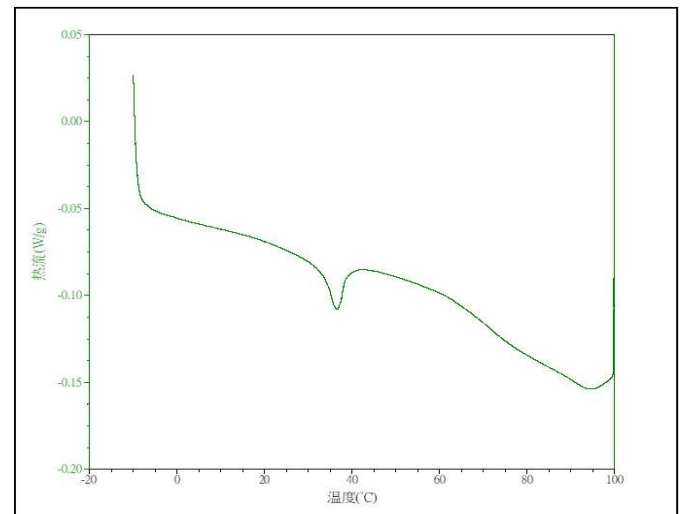


Fig.6: Photograph of SEM image (A&B)

In **Figure 5**, the compressive strength of cement mortar mixed with different amounts of paraffin at 3, 7, and 28 days is depicted. When the curing ages are 3, 7, and 28 days and the paraffin content is 20% and 25%, the compressive strengths of the cement mortar are 10.5% and 10.4% higher than those of the plain cement mortar, respectively. However, with a further increase in paraffin content, the compressive strength of the cement mortar does not increase and is lower than that of the plain cement mortar. This phenomenon is attributed to the uneven distribution of the paraffin within the mortar and the increased porosity. At a curing age of 28 days, the compressive strength of all the mixed cement mortar samples doped with paraffin is lower than that of the plain cement mortar. This could be due to the uneven dispersion of paraffin, which traps the flow of free water in the cement slurry, thereby reducing the degree of hydration.

SEM results: From **Figures 6 (a) and (b)**, it can be seen that the paraffin wax almost fills the circular sieve or long cylinder with a porous structure, indicating that the paraffin has been fully impregnated. The above demonstrates that this experiment successfully loaded paraffin into the expanded perlite using high-temperature and decompression adsorption methods.

DSC Curve analysis of paraffin samples:



The determination of the latent heat of the phase change of the sample involved setting the experimental temperature range from -20°C to 100°C. Liquid nitrogen was used to cool the sample to -20°C initially, followed by increasing the temperature at a rate of 5°C/min. The system automatically recorded the sample's curves and data on heat flow versus temperature. It was observed that peak temperatures and the overall curve shape of the phase-changing process were magnified by DSC testing

with higher heating and cooling rates. As the rate of heating or cooling rises, the hysteretic reaction is also accentuated. The melting point of paraffin was 39°C. The DSC curve of solid paraffin mortar is shown in **Figure 7**.

Thermal conductivity:

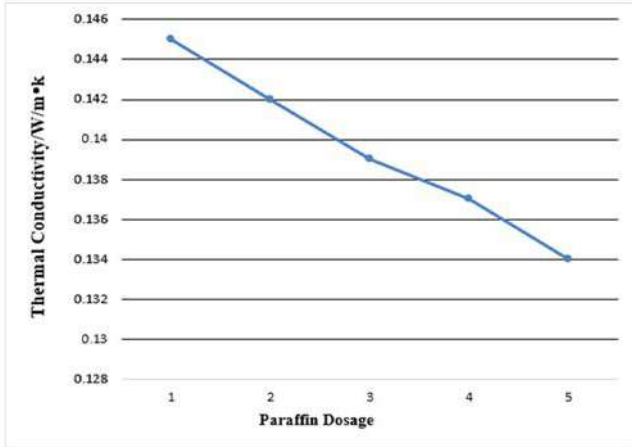


Fig.8: Photograph of Thermal conductivity of Paraffin sample

Figure 8 depicts that for thermal conductivity testing, a paraffin sample containing 20% paraffin was sent to the test centre. The specimen's dimensions were a diameter of 14.7 mm and a thickness of 2.32 mm. Data were collected at different temperatures. A material with low thermal conductivity does not easily transfer heat. Instead, it tends to insulate against heat flow, resisting the transfer of thermal energy. Materials with low thermal conductivity are often used as insulators to prevent heat loss or gain in various applications, such as building insulation, thermos flasks, and protective clothing. Low-thermal conductivity materials effectively resist heat transfer.

Thermal Control Effect Test:

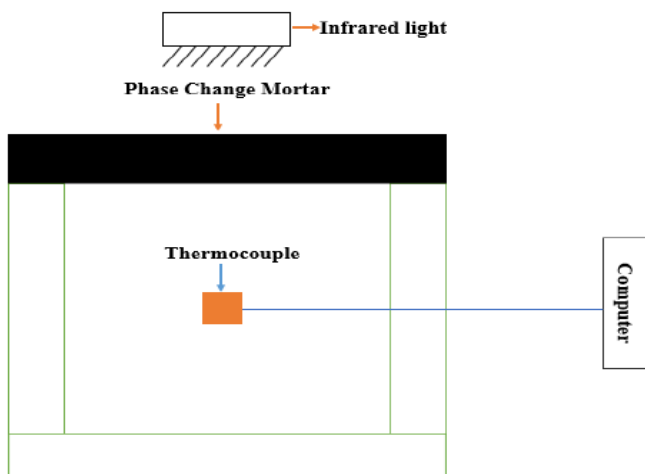


Figure-9: Photograph of Thermal Control Effect test

As depicted in Figure 9, the temperature adjustment performance test involves simulating the behaviour of phase-change materials under various environmental conditions to determine their effect on a house. To achieve this, a house model (Six panels are required to build a house or box) is constructed using mortar boards with panel top sides, each panel measuring 200*200*20 mm. The top side of the mortar board serves as the energy storage mortar board to be tested. High-efficiency infrared lamps are utilized for heating, while a thermometer records the temperature in the mortar model room. A sensor, consisting of a thermocouple, is placed at the centre of the house to sense temperature changes. The temperature-measuring thermocouple is connected to a computer via an ART Data Acquisition Module, DAM-3138, USB485/RS-422. Temperature software is used to control the infrared lamp heating process, and data on the indoor temperature control of the energy storage mortar is collected. Temperature data are collected every 10 minutes during the heating and cooling processes for graphing.

Temperature variation with Addition of Paraffin:

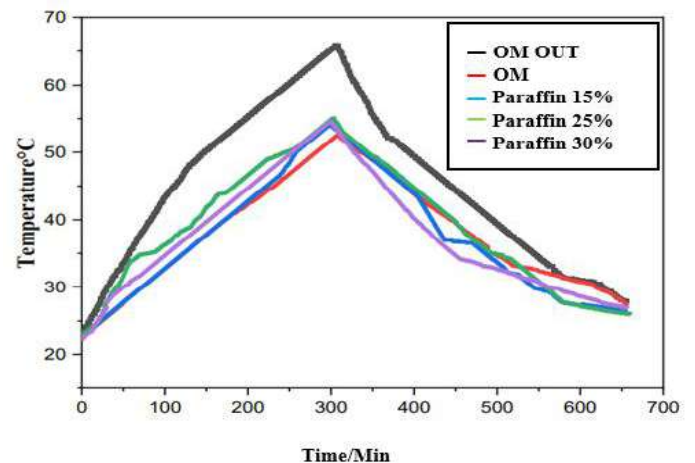


Fig.10: Photograph of Temperature variation with Addition of Paraffin

Figure 10 displays the quantity of paraffin composite phase change materials used in mortar rooms, along with a diagram illustrating the effect on the internal temperature of the house model. The temperature differences between paraffin-15%, paraffin-25%, and paraffin-30% are 19.69°C, 18.18°C, and 16.16°C, respectively, in comparison to the temperature of OM, while the temperature inside OM is 21°C relative to the outside temperature of OM.

Temperature Difference with Addition of Paraffin:

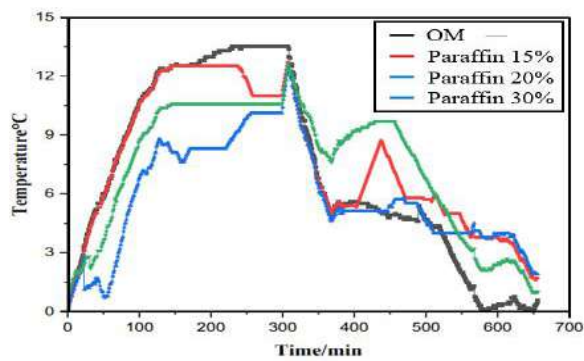


Fig.11: Photograph of Temperature Difference with Addition of Paraffin

Figure 11 depicts the temperature difference between ordinary mortar (OM) and paraffin composite phase change materials outside the house. The temperature differences for paraffin content of 15%, 25%, and 30% are 5.18°C, 7.4°C, and 9.6°C, respectively, while the temperature difference inside OM remains at 13.5°C.

VI. CONCLUSION

Based on the perspectives of energy saving, emission reduction, and building energy efficiency, this study examines paraffin. Its mechanical and thermal properties are tested, and the temperature adjustment performance test of the house model is determined. The effect of shape changes on the energy storage mortar board at room temperature is evaluated.

1. A paraffin mixture consisting of 20% and 25% was tested by DSC. It was found that the phase transition temperature of the paraffin wax mixture is 39°C, with a latent heat of phase transition of 111.5 J/g. Workability tests and thermal cycle tests indicate that the paraffin wax mixture exhibits good thermal stability and durability, rendering it suitable for use in building walls.
2. The expanded perlite, after acidification, exhibits numerous honeycomb pores capable of absorbing a significant amount of paraffin. Upon coating with calcium silicate powder, it demonstrates good thermal stability. Diatomite, after roasting and acidification treatment, primarily assumes a sieve-like and cylindrical shape, featuring high porosity and a large surface area. Additionally, it possesses nano-silica pores, making it an excellent porous adsorption material. Various porous materials can be utilized in the preparation of shape-fixed phase-change composites.
3. SEM results indicate that the expanded perlite experiences significant enhancement through heating and

vacuum adsorption, leading to increased absorption of the paraffin mixture. Infrared test results demonstrate that the adsorption process for both paraffins is purely physical, with no chemical reactions occurring. Upon encapsulation of the paraffin or expanded perlite with calcium terephthalate powder, a low exudation rate is observed, accompanied by excellent thermal stability. Additionally, the surface tension exhibits strong resistance to paraffin, preventing leakage and ensuring the binding force of the paraffin wax. Consequently, the prepared paraffin/expanded perlite and earth-set phase transition material exhibit stable performance, making them suitable for application in the field of building materials.

4. The phase-change energy storage mortar was prepared using both the intercalation method and the direct mixing method. With increasing dosage, the compressive strength, dry density, and thermal conductivity of the phase-change mortar gradually decreased. The performance of the phase-change energy storage mortar prepared using the intercalation method was superior to that of the phase-change energy storage mortar prepared using the direct mixing method. Even when the content is increased to 20%, the strength remains higher than 13.45 MPa, meeting the mechanical requirements for actual construction. Additionally, its thermal conductivity coefficient is extremely low, while the heat storage coefficient maintains a certain level, demonstrating good heat preservation and storage effects. Intercalation is thus identified as the preferred preparation process for phase-change energy storage mortar.

5. For the thermal control effect test, we found that the temperature was significantly lower than ordinary mortar when using paraffin.

ACKNOWLEDGMENT

Professor **Xiangyu Li** Faculty of Civil Engineering at Taiyuan University of Technology. He is grateful for the financial support for the study.

REFERENCES

- [1] Wang, X., Zhang, Y., Xiao, W., Zeng, R., Zhang, Q., & Di, H. (2009, March). Review on thermal performance of phase change energy storage building envelope. *Science Bulletin*, 54(6), 920–928.
- [2] Akeiber, H., Nejat, P., Majid, M. Z. A., Wahid, M. A., Jomehzadeh, F., Zeynali Famileh, I., Calautit, J. K., Hughes, B. R., & Zaki, S. A. (2016, July). A review on phase change material (PCM) for sustainable passive cooling in building envelopes. *Renewable and Sustainable Energy Reviews*, 60, 1470–1497.

- [3] Memon, S. A. (2014, March). Phase change materials integrated in building walls: A state of the art review. *Renewable and Sustainable Energy Reviews*, 31, 870–906.
- [4] Tyagi, V. V., & Buddhi, D. (2007, August). PCM thermal storage in buildings: A state of art. *Renewable and Sustainable Energy Reviews*, 11(6), 1146–1166.
- [5] Sharma, A., Tyagi, V., Chen, C., & Buddhi, D. (2009, February). Review on thermal energy storage with phase change materials and applications. *Renewable and Sustainable Energy Reviews*, 13(2), 318–345.
- [6] Oliver, A., Neila, F. J., & García-Santos, A. (2012, March 20). Clasificación y selección de materiales de cambio de fase según sus características para su aplicación en sistemas de almacenamiento de energía térmica. *Materiales De Construcción*, 62(305), 131–140.
- [7] Marani, A., & Nehdi, M. L. (2019, August). Integrating phase change materials in construction materials: Critical review. *Construction and Building Materials*, 217, 36–49.
- [8] Ling, T. C., & Poon, C. S. (2013, September). Use of phase change materials for thermal energy storage in concrete: An overview. *Construction and Building Materials*, 46, 55–62.
- [9] Zhang, D., Zhou, J., Wu, K., & Li, Z. (2005, March). Granular phase changing composites for thermal energy storage. *Solar Energy*, 78(3), 471–480.
- [10] Lee, T., Hawes, D., Banu, D., & Feldman, D. (2000, May). Control aspects of latent heat storage and recovery in concrete. *Solar Energy Materials and Solar Cells*, 62(3), 217–237.
- [11] Pongsopha, P., Sukontasukkul, P., Phoo-ngernkham, T., Imjai, T., Jamsawang, P., & Chindaprasirt, P. (2019, December). Use of burnt clay aggregate as phase change material carrier to improve thermal properties of concrete panel. *Case Studies in Construction Materials*, 11, e00242.
- [12] Bentz, D., Peltz, M., Durán-Herrera, A., Valdez, P., & Juárez, C. (2010, July 5). Thermal properties of high-volume fly ash mortars and concretes. *Journal of Building Physics*, 34(3), 263–275.
- [13] Du, Y., Liu, P., Quan, X., & Ma, C. (2020, September). Characterization and cooling effect of a novel cement-based composite phase change material. *Solar Energy*, 208, 573–582.
- [14] Xie, N., Niu, J., Zhong, Y., Gao, X., Zhang, Z., & Fang, Y. (2020, October). Development of polyurethane acrylate coated salt hydrate/diatomite form-stable phase change material with enhanced thermal stability for building energy storage. *Construction and Building Materials*, 259, 119714.
- [15] Essid, N., Eddhahak-Ouni, A., & Neji, J. (2020, September). Experimental and Numerical Thermal Properties Investigation of Cement-Based Materials Modified with PCM for Building Construction Use. *Journal of Architectural Engineering*, 26(3).
- [16] Singh Rathore, P. K., Shukla, S. K., & Gupta, N. K. (2020, February). Potential of microencapsulated PCM for energy savings in buildings: A critical review. *Sustainable Cities and Society*, 53, 101884.
- [17] ZETOLA VARGAS, V., GARCÍA SANTOS, A., & NEILA GONZÁLEZ, F. J. (2013, April). Mortero de Cemento Portland con parafinas microencapsuladas. *Revista De La Construcción*, 12(1), 75–86.
- [18] Jayalath, A., San Nicolas, R., Sofi, M., Shanks, R., Ngo, T., Aye, L., & Mendis, P. (2016, September). Properties of cementitious mortar and concrete containing micro-encapsulated phase change materials. *Construction and Building Materials*, 120, 408–417.
- [19] Haurie, L., Serrano, S., Bosch, M., Fernandez, A. I., & Cabeza, L. F. (2016, January). Single layer mortars with microencapsulated PCM: Study of physical and thermal properties, and fire behaviour. *Energy and Buildings*, 111, 393–400.
- [20] Norvell, C., Sailor, D. J., & Dusicka, P. (2013, July). THE EFFECT OF MICROENCAPSULATED PHASE-CHANGE MATERIAL ON THE COMPRESSIVE STRENGTH OF STRUCTURAL CONCRETE. *Journal of Green Building*, 8(3), 116–124.
- [21] Cunha, S., Lima, M., & Aguiar, J. B. (2016, November). Influence of adding phase change materials on the physical and mechanical properties of cement mortars. *Construction and Building Materials*, 127, 1–10.
- [22] Xu, B., & Li, Z. (2013, May). Paraffin/diatomite composite phase change material incorporated cement-based composite for thermal energy storage. *Applied Energy*, 105, 229–237.
- [23] Li, X., Sanjayan, J. G., & Wilson, J. L. (2014, June). Fabrication and stability of form-stable diatomite/paraffin phase change material composites. *Energy and Buildings*, 76, 284–294.
- [24] Zhang, Z., Shi, G., Wang, S., Fang, X., & Liu, X. (2013, February). Thermal energy storage cement mortar containing n-octadecane/expanded graphite composite phase change material. *Renewable Energy*, 50, 670–675.
- [25] Li, H., Chen, H., Li, X., & Sanjayan, J. G. (2014, December). Development of thermal energy storage composites and prevention of PCM leakage. *Applied Energy*, 135, 225–233.
- [26] Pilehvar, S., Cao, V. D., Szczotok, A. M., Valentini, L., Salvioni, D., Magistri, M., Pamies, R., & Kjøniksen, A. L. (2017, October). Mechanical properties and microscale changes of geopolymer concrete and Portland cement concrete containing micro-encapsulated phase change materials. *Cement and Concrete Research*, 100, 341–349.
- [27] Brazão Farinha, C., de Brito, J., & Veiga, R. (2019, October). Influence of forest biomass bottom ashes on the fresh, water and mechanical behaviour of cement-based mortars. *Resources, Conservation and Recycling*, 149, 750–759.
- [28] Kuznik, F.; David, D.; Johannes, K.; Roux, J.J. A review on phase change materials integrated in building walls. *Renew. Sustain. Energy Rev.* 2011, 15, 379-391.
- [29] da Cunha, S. R. L., & de Aguiar, J. L. B. (2020, February). Phase change materials and energy efficiency of buildings: A review of knowledge. *Journal of Energy Storage*, 27, 101083.
- [30] Cunha, S., Leite, P., & Aguiar, J. (2020, August). Characterization of innovative mortars with direct incorporation of phase change materials. *Journal of Energy Storage*, 30, 101439.

- [31] Wang, H., Lu, W., Wu, Z., & Zhang, G. (2020, January). Parametric analysis of applying PCM wallboards for energy saving in high-rise lightweight buildings in Shanghai. *Renewable Energy*, 145, 52–64.
- [32] Kishore, R. A., Bianchi, M. V., Booten, C., Vidal, J., & Jackson, R. (2020, November). Optimizing PCM-integrated walls for potential energy savings in U.S. Buildings. *Energy and Buildings*, 226, 110355.
- [33] Saafi, K., & Daouas, N. (2019, November). Energy and cost efficiency of phase change materials integrated in building envelopes under Tunisia Mediterranean climate. *Energy*, 187, 115987.
- [34] Ye, R., Huang, R., Fang, X., & Zhang, Z. (2020, January). Simulative optimization on energy saving performance of phase change panels with different phase transition temperatures. *Sustainable Cities and Society*, 52, 101833.

Numerical Study of Casson Nanofluid Flow over a Stretching Surface

Usama¹, Muhammad Amad Sarwar^{2*}, Muhammad Awais¹, Muhammad Mukhtar Khan³,
Ioannis Sarris⁴

¹Department of Mathematics, University of Sialkot, Sialkot, Punjab province, Pakistan. (usamamathematician44@gmail.com, awaisahi9137@gmail.com)

^{2*}School of Mathematics, Nanjing University of Aeronautics and Astronautics, Nanjing, Jiangsu province, 211106, PR China. (m.amadsarwar26@gmail.com)

³School of Mathematics International Islamic University, Islamabad, Pakistan (shahzaib995995@gmail.com)

⁴Department of Mechanical Engineering, University of West Attica, Greece. (sarris@uniwa.gr)

Received: 09 Feb 2024,

Receive in revised form: 22 Mar 2024,

Accepted: 07 Apr 2024,

Available online: 14 Apr 2024

©2024 The Author(s). Published by AI
Publication. This is an open access article
under the CC BY license

(<https://creativecommons.org/licenses/by/4.0/>)

Keywords— Casson nanofluid, Stretching surface, Thermal radiation effects, Keller box methodology, Reduced Sherwood number

Abstract— In this contribution, the numerical analysis of the Casson nanofluid towards a stretching surface is studied. The stagnation flow with thermal radiation effects over an exponentially stretching has been considered. The flow problem governing partial differential equations are converted into the ordinary differential equations along with relevant boundary conditions using appropriate similarities. The resulting ODEs then solved numerically using the Keller box methodology, which is a well-known technique. It can be shown from the comparison that our current results and the earlier ones have a good match. It has been found that the reduced Sherwood number, increases for increasing values of radiation parameter while, Nusselt number and skin friction coefficient decreases. Furthermore, the skin-friction coefficient increases as the inclination factor increases but Nusselt and Sherwood numbers decline. The temperature profile increases with the increasing behavior of radiation factor. Further the magnetic effects reduce the velocity profile.

LIST OF SYMBOLS

u, v	Velocity component in x, y directions	D_B	Brownian diffusion coefficient
T	Local nanofluid temperature	D_T	Coefficient of thermophoretic diffusion
β	Casson fluid parameter	η	Similarity variable
C	Local nanoparticle concentration	M	magnetic field
T_w	Constant disk temperature	R	disk of radius
T_∞	Temperature of the ambient nanofluid's,	τ	Shear stress
C_∞	Ambient nanoparticle concentration	Pr	Prandtl number
P	Nanofluid pressure	Sc	Schmidt number
P_∞	pressure of the ambient nanofluid	Nb	Brownian motion parameter
ω	angular velocity	Nt	thermophoresis parameter
α_f	Thermal diffusivity of base fluid	B_0	Magnetic field strength
		Nu	Local Nusselt number

C_{fx}	Skin friction coefficient
R_e	Reynolds number
N	Radiation parameter
ν	Kinematic viscosity of the fluid
θ	Dimensionless temperature
ϕ	Dimensionless concentration
ρ	Density of the fluid
σ	Electrical conductivity of the fluid
L	Characteristic length
k	Thermal conductivity

I. INTRODUCTION

A fluid is a substance which is capable of flowing and deforms continuously under the action of shearing stress. Fluid mechanics can be defined as the study of fluid's behavior at rest and in motion. It consists of three parts which are fluid statistics, fluid dynamics and fluid kinematics which deals with the fluids at rest, fluids in motion and the fluids in motion where pressure energy is not considered respectively. If a fluid contains microscopic quantities of nanoparticles or nano fibers, which have a diameter less than 100 nm then it is termed as Nanofluid. Emerging energy transfer base liquids including H₂O, toluene, and motor oil are mixed with nanoparticles or Nano fibers to create Nano fluids. Base fluid's thermal conductivity can be increased by adding nanoparticles which results in increasing the nanofluid's natural convection heat transfer in comparison with base fluid. Nanofluids have distinctive properties due to which they can be used in a range of heat transfer applications i.e., microelectronics, pharmaceutical processes, domestic refrigerators, coolers and fuel cells, heat exchangers and hybrid engines having higher thermal conductivity and lower convective heat transfer coefficients as compared to base fluids. To improve thermal conductivity of these fluids, nano- or micron-sized particles are added which allows them to transfer more heat. The time-independent flow of non-Newtonian liquids through tubes with fixed yield values has attracted more attention recently due to their applications in the polymer processing industry and in biofluid dynamics. The most common fluid is Casson fluid. A Casson fluid can be defined as a shear-thinning liquid assuming infinite viscosity at zero shear rate, no flow below the yield stress, and zero viscosity at infinite shear rate.

In fluid dynamics, the term stagnation point termed as the point at which the local velocity of fluid is zero. When fluid is not in motion on the surface of an object, there is stagnation point in the flow field.

Newtonian fluids are as those fluids which have shear stress proportional to the rate of shear strain. Those fluids which obey the newtons law termed as Newtonian fluids which include air, thin motor oil, glycerol, and water.

Non-Newtonian fluids are those which do not obey Newton's law in which shear stress and deformation rate are not linear. The term viscous force is the frictional force that prevents different fluid layers from sliding. Whereas the measure of resistance of the fluid relative to the fluid's motion is termed as viscosity. Non-Newtonian fluids present special challenges to engineers, mathematicians, and physicists. Non-Newtonian examples are starch suspensions, shampoos, melted butter, etc.

Magnetohydrodynamics (MHD) also known as magnetohydrodynamics, or fluid magnetism is the study of the magnetism and behavior of conducting fluids. Few examples are plasmas, brines, liquid metals, and electrolytes. The root of the term magnetohydrodynamics is magneto, which means magnetic field and hydro which indicates water, and dynamics, which indicates motion. Magnetohydrodynamics was discovered by Hannes Alfvén for which he received the Nobel Prize in Physics in 1970. The idea behind magnetohydrodynamics is that a magnetic field can induce a current in a flowing conductive fluid, which polarizes the fluid, which in turn changes the magnetic field. The Navier-Stokes equations of hydrodynamics combined with the Maxwells equations of electromagnetism provide a set of equations that describe magnetohydrodynamics. These differences must be resolved simultaneously, both analytically and numerically.

A nanoparticle is a very small particle that has a diameter between 1 and 100 nanometers. Since they are too small to be seen with the human eye, nanoparticles can differ significantly from larger materials in terms of their physical and chemical properties. A fluid called a nanofluid contains particles, also known as nanoparticles, that are smaller than a nanometer. Its most utilized in polymer processing, fiber sheets making, and in drilling etc. In current era non-Newtonian liquid gain especial intensions of researchers because of the applications. Casson liquid is a type of the non-Newtonian liquids which has infinite viscosity against zero shear stress and vice versa. The famous examples of Casson liquid are blood, fruit, juices, ketchup etc. In nanofluids, nanoparticles are frequently formed of oxides, carbon nanotubes, metals, or carbides.

Due to its importance in engineering and industry, including the production of materials by extrusion, glass fiber production, hot rolling, extrusion of rubber and plastics, and the extrusion of polymer sheets, many researchers have focused on extending the tensile surface on the flow (Khan and Pop., 2010). Sakiadis (1961) was the first to explore

laminar boundary layer flow of viscous and incompressible fluids induced by constantly moving rigid bodies. Crane (1970) discussed flow towards a stretching surface based on the research of Sakiadis. Khan and Pop analyzed nanofluid's flow onto stretching surface by incorporating additional properties such as Brownian motion and thermophoresis (2010).

The boundary layer approximation was initially used to evaluate the surface stretching issue by Sakiadis. For a stretched sheet, Crane established a precise solution of the two-dimensional Navier-Stokes equations in analytical form. Gupta looked at the Crane's suction/injection issue at the wall. Prandtl (1874–1953) reported his work on the motion of fluids with very little friction in his paper. Prandtl introduced the idea of a boundary layer, which eventually changed how viscous flows were analyzed in the century of twenty.

By presenting viscosity of fluids, Prandtl has given fluid mechanics a new way. Prandtl's boundary layer idea, viscous forces have a substantial influence in the thin region to the surface of the velocity gradient, but the viscous forces are negligible from the surface of discovered field flow. Because of the viscous forces, the surface connected to the surface has no velocity. It's called as "no slip" condition. Due to its thinness, the boundary layer plays an important role in fluid dynamics. It has full-grown into a useful tool for studying the behavior of real fluids.

The boundary layer idea simplifies Navier-Stokes equations to the point that they may be utilized to investigate a vast range of real-world issues. Because boundary layer equations are parabolic, so the boundary layer theory is critical for solving fluid and heat transport issues. The entire Navier-Stokes equations, on the other hand, are elliptic in nature, even though they are often hyperbolic, and much more complicated. As a result, the boundary layer equation is significantly easier to solve (Schlichting et al., 1960).

According to Newton's law of viscosity, "shear stress is exactly proportional to velocity gradient".

Numerically it can be expressed as

$$\tau \propto \frac{du}{dy} \quad (1.1)$$

$$\tau = \mu \frac{du}{dy} \quad (1.2)$$

When the temperatures of two things differ, heat is transferred from one to the other. The movement of internal energy from one substance to another that is at a different temperature is known as heat transfer. The following three strategies are used to create this heat mechanism.

Conduction is the heat transmission mechanism that occurs when molecules and atoms collide directly.

Heat is transferred by mass transfer or actual molecular movement. It is divided into three categories.

Natural convection is a mass and heat transmission technique where fluid motion is exclusively brought about by changes in the fluid's density, not by any outside force (like a pump and fan).

An external source is used to compel fluid molecules to flow in forced convection.

Mixed convection is the most frequently used type of convection when natural and free convection work together in heat transmission. When the buoyancy and external forces interact, this phenomenon occurs.

Radiation is a type of heat transmission that happens when electromagnetic waves are emitted and does not require a medium to propagate. When it comes to heat transmission in liquids and gases, radiation and convection are important, while heat transfer in solid materials is handled by conduction. The most common example of radiation is heat emitted by a fire.

It measures the proportion of inertial to viscous forces. Based on their behavior, fluid flows can be categorized as laminar or turbulent. Mathematically it can be expressed as below

$$R_e = \frac{\text{Inertial forces}}{\text{Viscous forces}} \quad (1.5)$$

$$R_e = \frac{Lc}{\nu} \quad (1.6)$$

where c represents velocity, L represents characteristic length, and ν represents kinematic viscosity. Reynolds number is a non-dimensionlized number.

This study focuses on the numerical analysis of Casson nanofluids on stretched surfaces, inspired by the applications mentioned in the previous section. This flow behavior towards stretched surfaces has been studied by many researchers. Extensive surface geometries for Casson Nano fluids are understudied. Therefore, this study focuses on the mass and heat transfer of Casson Nano fluids on stretched surfaces.

This research may address the relationship between the existing Navier-Stokes models that depict the behavior of boundary layer flow and Casson nanofluid models.

Research objectives and Research Questions

The objective of this study is the numerical development of mass and heat transfer in casson nanofluids flowing towards stretching surface in a magnetohydrodynamic boundary layer. The following objectives will be the focus of this work:

- i. To study of stagnation point flow of Casson nanofluids flowing on an inclined surface.

The numerical results of the transfer of the heat and the mass's magneto hydrodynamic boundary layer flow of Casson nanofluid towards a stretching surface is presented in this study. Due to its numerous applications in industry, the heat, and the mass transmission MHD boundary layer flow across an exponentially extending surface has gotten a lot of attention. Furthermore, such flows have numerous applications in electrochemistry, chemical engineering, and polymer processing.

II. REVIEW OF LITERATURE

(Kouz et al., 2022) studied the rotating frame of references characteristics of heat transfer and three-dimensional flow of Non-Newtonian Nano liquid over a stretched surface. (Tayebi et al., 2022) reported a numerical study in an inclined I-shaped enclosure with two heated cylinders, thermal free convection of micropolar nanofluid and the production of entropy. They found that the rate of heat exchange increased when the Rayleigh (Ra) and geometric aspect ratio (AR) parameters increased but decreased when the vertex viscosity parameter(K) increased. (Gaurav Gupta et al., 2022) examined the radially extended infinite gyrate-induced 3D (three dimensional) magneto stagnation point flow of hybrid nanofluid. Non-Newtonian fluid's boundary layer flow and heat transfer to anextending surface when the surface is suctioned or blown. (Manan et al., 2021) described the investigation of non-Newtonian fluid flow of the Casson type through heat & mass conduction in direction of stretching surface with thermophoresis and radiation absorption interactions with hydromagnetic effect. (Rafique et al., 2019) examined an inclined surface having Soret and Dufour effects, and impact of boundary layer flow of casson nanofluid. (Awais et al., 2021) investigated the effect of heat generation and Lorentz force reducing walls on MHD (magnetohydrodynamic) flow of Casson fluids through porous media. (Rafique et al., 2022) used a computational model to study the energy and mass transport behavior of a micro rotating flow through a Riga plate, considering suction or injection as well as mixed convection. They found that when mass transfer increased, heat transfer across the surface decreased by a temperature stratification factor. In addition, as the modified Hartmann number increased, the fluid velocity also increased. (Hussain et al., 2022) used a fluid model to undertake numerical analysis on time-dependent, incompressible electrically conducting squeezing flow of Casson liquid. The non-Newtonian fluid was contained between two discs, one stationary and the other moving up and down. Slip parameters were found to decrease the Nusselt and Sherwood numbers on both discs. (Fatunmbi et al., 2022)

investigated hydromagnetic Casson nanofluid flow via a nonlinear stretchy sheet and generated entropy using Navier slips. The results demonstrated that when the Brownian motion was increased, the momentum boundary layer improved while the concentration distribution decreased. (Rafique et al., 2019) by combining the influences of chemical reaction and heat generation, Casson Nanofluid boundary layer stream over linear slanted extending sheet was developed. With the help of convective borders and thermal radiations, Brownian motion, and thermophoresis diffusion on Casson nanofluid boundary layer flow along a nonlinear inclined stretching sheet was also reported by (Rafique et al., 2019). Considerations are being given to Casson nanofluid flow over a nonlinear, titled, extended sheet with impacts from chemical reactions and heat generation/absorption by (Anwar et al., 2021). (Almakki et al., 2021) investigated the Casson nanofluid model equations for MHD fluids in the presence of entropy formation and chemical reactions on a stretching surface boundary layer. Thermal and mass transfer is detected due to solutal and thermal stratification, heat ratio and viscous dissipation. (Chand et al., 2021) explored theoretical effects of thermal convection in horizontal layers of micropolar nanofluids. (Khan et al., 2022) studied the steady, non-Newtonian Casson fluid motion characteristics of heat and mass transfer over a permeable medium through a stretching surface impact of heat creation and thermal emission. (Atif et al., 2021) examined how a magneto hydrodynamic Casson nanofluid behaved as it was passed over a stretching sheet. Non-Fourier and non-Fick's models were used in all the calculations. (Ramesh et al., 2021) investigated the incompressible and time-dependent squeezing flow of Casson and micropolar nano fluid. (Mustafa et al., 2011) explained the direction of a stretching sheet by a Casson fluid flow in its stagnation point area. Additionally examined are the parameters of heat transmission with viscous dissipation. Heat transfer and flow are represented by partial differential equations. Fazle Mehboob concentrated on the farming of melting heat transfer on magnetohydrodynamic (MHD) Casson fluid flow in a porous media under thermal radiation's effect. (Xu et al., 2022) investigated the use of a transparent nanofluid (Au) with high thermal conductivity to achieve better convective thermal management of optoelectronic devices. The heat conductivity of the Au nanofluid was improved by 50% while exhibiting stable dispersion. A statistical analysis of studies using artificial neural networks to predict the thermophysical properties of nanofluids was carried out by (Este et al., 2022). Investigation of all factors influencing the thermal conductivity of nanofluid, including base fluid type, nanoparticle type, particle concentration, fluid temperature, fluid stability, and others. Experimental

research was done to determine the thermal conductivity of various forms of nanoparticles in nano fluids by (Cui et al., 2022). (Lund et al., 2020) emphasized the heat transport features of a convective micropolar nanofluid on a permeable shrinking stretching inclined surface. Over a moving surface, (Khan et al., 2020) described a magnetized Casson nanofluid and motile microorganism with changing heat conductivity. A second-grade fluid model and a refined variant of the Casson fluid model were used to develop the mathematical modeling. (Cui et al., 2022) explored whether introducing Janus particles would improve the thermal conductivity of nanofluid. (Ullah et al., 2021) explored for the numerical treatment of Maxwell nanofluid thin film flow on a stretched and rotating surface, intelligent computer networks are designed. Using the Buongiorno model, the thermophoretic and Brownian motion characteristics of nanofluid were found. By slandering the surface (Hayat et al., 2018) research was done on MHD stratified nanofluid flow. They found that modifying thermal conductivity and the Hartmann number enhances temperature dispersion. According to a paper, Arrhenius activation energy and heat radiation have an impact on how entropy is produced in nonlinear mixed convective nano fluid flow in porous space by (Alsaadi et al., 2020). In the early 1900s, German scientist Ludwig Prandtl presented the hypothesis that defines boundary layer effects studied by (Anderson et al., 2005). (Rehman et al., 2022) conducted a thermal case study for radial stagnation point flow to examine heat transmission factors. For the positive iteration in torsional rate., it was observed that the temperature gradient awed very minor fluctuation. (Gbadeyan et al., 2020) explores the impact of combination variable viscosity and thermal conductivity, nonlinear radiations. With higher values of variable thermal conductivity and viscosity, it was discovered that velocity rises while temperature and the volume fraction of nanoparticles fall. (Jamshed et al., 2022) studied the energy transfer and entropy of a non-Newtonian Casson fluid flow that was unstable. By exposing the nanofluid to a slippery surface that is convectively heated, its flow and heat transport characteristics were examined. They adopted a numerical technique named as Keller box technique. (Alwawi et al., 2020) examine how a magnetic field affects the free convection of an ethylene glycol based on Casson fluid as it revolves around a circular cylinder. The magnetohydrodynamic free convective flow of Casson

nanofluid was examined using Tiwari & Das's nanofluid model. (Jamshed et al., 2021) examined the heat transport and entropy of a non-Newtonian Casson nanofluid in unsteady flow. The model equations for casson nanofluid flow and heat transfer are compressed using boundary layer flow and the Roseland approximation. (Alwawi et al., 2020) investigated the MHD free convective flow of sodium alginate nanofluid over solid spheres with specified wall temperatures. The Nano fluid model developed by Tiwari and Das was used to examine how a magnetic field and nanoparticles affected a naturally occurring convective flow.

III. RESEARCH METHODOLOGY

The movement of a Casson nanofluid toward an exponential stretching surface is covered in this chapter. This section's primary goal is to explore the flow behavior of a Casson nanofluid approaching a sheet that is stretching exponentially. By using boundary layer approach, the mathematical formulation is obtained. By applying an appropriate transformation, the relevant boundary layer equations are reduced into the coupled nonlinear ODE's. A detailed study is accomplished to approach the impacts of interesting parameters on non-dimensional velocity, temperature distribution and concentration. The coefficient of C_f , Nu, and Sh are also computed numerically.

Problem Formulation

We examine a Casson nanofluid's two-dimensional stagnation-point flow toward a slanted exponentially stretching sheet. The free stream and stretching velocities are taken to have the formulas $u = u_w(x) = ae^{x/l}$ and $u \rightarrow u_\infty(x) = be^{x/l}$ where x is the location taken along the stretching surface, a and b are constants. Along with nanoparticles, the base fluid also contains rotating Casson finite-sized particles. The fluid molecules in the Casson nanofluid have more room to move before colliding into one another, This results in gyration effects due to the molecules' rotation in the fluid continuum. At the wall, T and C remain constant and are denoted by the letters T_w and C_w , where T stands for temperature and C for the nanoparticle fraction. Furthermore, figure (3.1) shows that the ambient values when y goes to infinity are C_∞ and T_∞ .

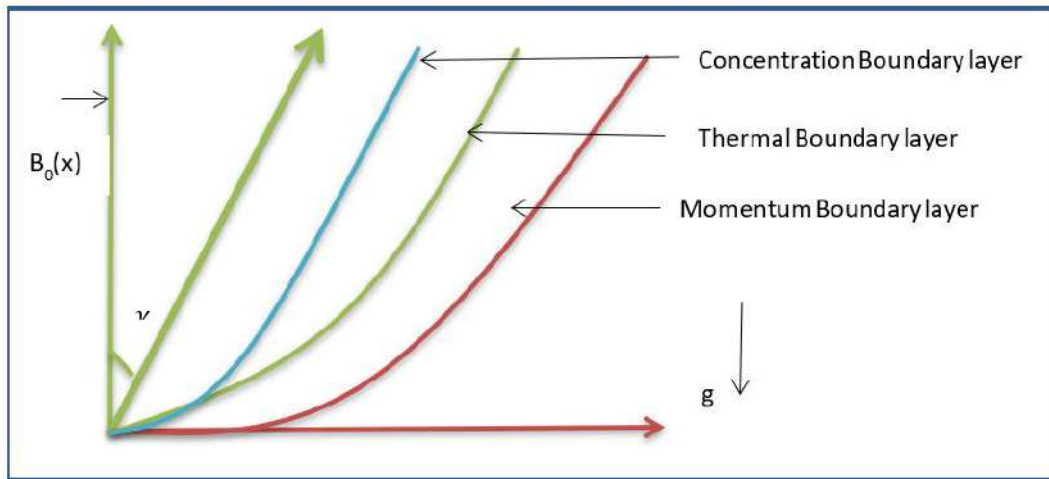


Fig.3.1. Coordinate System and Physical Model

The governing equations into the following forms:

$$\frac{\partial u}{\partial x} + \frac{\partial v}{\partial y} = 0, \tag{3.1}$$

$$u \frac{\partial u}{\partial x} + v \frac{\partial u}{\partial y} = u_\infty \frac{du_\infty}{dx} + v \left(1 + \frac{1}{\beta} \right) \frac{\partial^2 u}{\partial y^2} + \frac{\sigma B^2}{\rho} (u_\infty - u) + g [B_t (T - T_\infty) + B_c (C - C_\infty)] \cos \omega, \tag{3.2}$$

$$u \frac{\partial T}{\partial x} + v \frac{\partial T}{\partial y} = \alpha \frac{\partial^2 T}{\partial y^2} - \frac{1}{(\rho c)_f} \frac{\partial q_r}{\partial y} + \tau \left[D_B \frac{\partial C}{\partial y} \frac{\partial T}{\partial y} + \frac{D_T}{T_\infty} \left(\frac{\partial T}{\partial y} \right)^2 \right], \tag{3.3}$$

$$u \frac{\partial C}{\partial x} + v \frac{\partial C}{\partial y} = D_B \frac{\partial^2 C}{\partial y^2} + \frac{D_T}{T_\infty} \frac{\partial^2 T}{\partial y^2}. \tag{3.4}$$

Simplify (3.3), which reduces the radiative heat flux to:

$$q_r = \frac{-4\sigma^* \partial T^4}{3k^* \partial y} \tag{3.5}$$

where the mean absorption coefficient and the Stefan-Boltzmann constant, respectively, are denoted by k^* and σ^* . Without considering higher-order terms, In a Taylor series concerning T_∞ , expanding T^4 yields:

$$T^4 = 4T_\infty^3 T - 3T_\infty^4$$

Thus, simplified form of equation (3.3) is

$$u \frac{\partial T}{\partial x} + v \frac{\partial T}{\partial y} = \alpha \left(1 + \frac{4N}{3} \right) \frac{\partial^2 T}{\partial y^2} + \tau \left[D_B \frac{\partial C}{\partial y} \frac{\partial T}{\partial y} + \frac{D_T}{T_\infty} \left(\frac{\partial T}{\partial y} \right)^2 \right], \tag{3.6}$$

where the velocity components in the x and y directions are both v and u, respectively, ρ is the base fluid's density, μ is the viscosity, σ is the electrical conductivity, $\alpha = \frac{k}{(\rho c)_f}$ is the thermal diffusivity parameter where $(\rho c)_f$ is the base fluid's heat capacity and k is known as thermal conductivity, N represents radiation parameter, $\tau = \frac{(\rho c)_p}{(\rho c)_f}$ is the relation between nanoparticle's effective heat capacity and heat capacity of liquid, furthermore, D_T stands for thermophoresis diffusion coefficient and D_B stands for Brownian motion.

Boundary conditions that are imposed are listed below.

$$u = u_w(x) = ae^{x/l}, v = 0, T = T_w(x), C = C_w(x) \text{ at } (y = 0)$$

$$u \rightarrow u_\infty = be^{x/l}, v \rightarrow 0, T \rightarrow T_w, C \rightarrow C_w \text{ as } y \rightarrow \infty. \tag{3.7}$$

In order to convert the nonlinear PDE into nonlinear ODE, a similarity transformation is defined. Where, the stream function is $\psi = \psi(x, y)$.

$$u = \frac{\partial \psi}{\partial y}, v = -\frac{\partial \psi}{\partial x}. \tag{3.8}$$

The exponentially stretching sheet velocity is used to define the similarity transformation as follows:

$$\psi = \sqrt{2lva}e^{\frac{x}{2l}}f(\eta), \theta(\eta) = \frac{T - T_\infty}{T_w - T_\infty}, \phi(\eta) = \frac{C - C_\infty}{C_w - C_\infty}, \tag{3.9}$$

Where,

$$T_w(x) = T_\infty + T_0e^{\frac{2x}{l}}, C_w = C_\infty + C_0e^{\frac{2x}{l}}.$$

Eqs. (3.2 - 3.4) are reduced to nonlinear ODE when Eq. (3.9) is substitute

$$\left(1 + \frac{1}{\beta}\right)f''' + ff'' - 2f'^2 + 2\gamma^2 + M(\gamma - f') + (\lambda\theta + \delta\phi)Cos\omega = 0, \tag{3.10}$$

$$\left(1 + \frac{4}{3}N\right)\theta'' + (\theta'f - \theta f' + Nb\theta'\phi' + Nt\theta'^2)Pr = 0, \tag{3.11}$$

$$\phi'' + Le(\phi'f - \phi f') + \frac{Nt}{Nb}\theta'' = 0, \tag{3.12}$$

Where

$$\gamma = \frac{b}{a}, Pr = \frac{\nu}{\alpha}, Le = \frac{\nu}{D_B}, M = \frac{2l\sigma B^2}{a\rho}, K = \frac{k_1^*}{\mu}, Nb = \frac{D_B\tau(C_w - C_\infty)}{\nu}, Nt = \frac{\tau D_T(T_w - T_\infty)}{\nu T_\infty}, Nt_b = \frac{Nt}{Nb}, \lambda = \frac{G_r}{Re_x^2}, G_r = \frac{2gB_t(T_w - T_\infty)l^3}{\nu^2}, \delta = \frac{G_c}{Re_x^2}, G_c = \frac{2gB_c(C_w - C_\infty)l^3}{\nu^2}, Le = \frac{\nu}{D_B}, N = \frac{4\sigma T_\infty^3}{kk^*}. \tag{3.13}$$

Here, prime stands for derivative w.r.t η , M is the magnetic parameter known as the Hartmann number, Pr (Prandtl number), K is the dimensionless vortex viscosity, γ is the velocity ratio parameter, N is the radiation parameter, ν is the kinematic viscosity of the fluid, Le is the Lewis number, $Nt_b = \frac{Nt}{Nb}$ where Nt is the thermophoresis parameter and Nb is the Brownian motion parameter, λ is the buoyancy parameter, G_r is the local Grashof number, δ is the solutal buoyancy parameter, G_c is the local solutal Grashof number, Sc is the Schmidt number.

The imposed boundary conditions (3.7) are transformed to

$$f(\eta) = 0, f'(\eta) = 1, \theta(\eta) = 1, \phi(\eta) = 1 \text{ at } \eta = 0, \\ f'(\eta) \rightarrow \gamma, \theta(\eta) \rightarrow 0, \phi(\eta) \rightarrow 0 \text{ as } \eta \rightarrow \infty. \tag{3.14}$$

The (Sh) for Sherwood number, (Nu) for Nusselt number and (C_f) for skin friction are defined as below:

$$Sh = \frac{xq_m}{D_B(C_w - C_\infty)}, Nu = \frac{xq_w}{k(T_w - T_\infty)}, C_f = \frac{\tau_w}{\rho u_w^2}. \tag{3.15}$$

Where $\tau_w = (\mu + k_1^*)\frac{\partial u}{\partial y} + k_1^*N^*$, $q_m = -D_B\frac{\partial C}{\partial y}$ and $q_w = -k\frac{\partial T}{\partial y}$ at $y = 0$ are the mass and heat fluxes and shear stress at the surface, respectively. The reduced Sherwood number $- \phi'(0)$, reduced Nusselt number $- \theta'(0)$, and skin friction coefficient $C_{fx}(0) = \left(1 + \frac{1}{\beta}\right)f''(0)$ are linked expressions that are defined as follows:

$$C_{fx}(0) = C_f\sqrt{Re_x}, -\theta'(0) = \frac{Sh}{\sqrt{Re_x}}, -\theta'(0) = \frac{Nu}{\sqrt{Re_x}}. \tag{3.16}$$

Here $Re_x = \frac{ax e^{x/L}}{\nu}$ is the Local Reynolds number.

IV. RESULTS AND DISCUSSION

The Keller-box approach is used in chapter 3 to solve the transformed nonlinear ODE's (3.10–3.12) that are subjected

to BC's (3.14). The results for the relevant physical parameters, such as Nb, Pr, M, N, ω , δ , Nt, Le, β , λ , and γ are presented in tabular form by using table 4.1 and 4.2.

When δ , Nt , β , γ , Nb , λ , and Le are equal to zero and $\omega = 90^\circ$. Table 4.1 compares the current findings for the reduced Nusselt number $\theta'(0)$ to the findings from Bidin and Nazar (2009) and Ishak (2011). To illustrate how $\theta'(0)$, $\phi'(0)$, and C_{fx} vary for various values of N , M , δ , ω , Nt , Le , Nb , β , Pr , λ and γ , Table 4.2 is constructed. It has been found that when Nb , Le , N , Nt , M and ω are increased, $\theta'(0)$ grows, whereas Pr , λ , γ , β and δ are increased, $\theta'(0)$ lowers. The table, however, clearly demonstrates that the local Sherwood number $\phi'(0)$ is decreasing while rising,

ω , Le , and M . While rising with increasing values of Pr , N , γ , β , Nt , Nb , δ , Le , λ . Additionally, it has been discovered that the skin friction coefficient $C_{fx}(0)$ decreases as Nt , λ , γ , N , δ and increases when Nb , Le , ω , Pr , M , and β values rise. The negative values of $C_{fx}(0)$ signify a drag force being applied to the motions of the micropolar nanofluid by the stretching sheets. This is not unexpected considering that stretching is the only factor responsible for the boundary layer's development. It can be seen from this table that the increasing value of γ .

Table 4.1: Comparison of $-\theta'(0)$ (local Nusselt number) when Nb , Pr , γ , β , Nt , Le , $\sigma=0$ and $\omega=90^\circ$

Pr	M	N	Bidin and Nazar (2009) $-\theta'(0)$	Ishak (2011) $-\theta'(0)$	Present Results $-\theta'(0)$
1	0	0	0.9548	0.9548	0.9548
2	0	0	1.4714	1.4714	1.4714
3	0	0	1.8691	1.8691	1.8691
1	0	1.0	0.5315	0.5312	0.5312
1	1.0	0	-	0.8611	0.8611
1	1.0	0	-	0.4505	0.4505

Table 4.2: Value of $-\theta'(0)$, $-\phi'(0)$ and $C_{fx}(0)$.

Nb	Nt	Pr	Le	M	β	N	Λ	σ	γ	ω	$-\theta'(0)$	$-\phi'(0)$	$-\theta'(0)$
0.1	0.1	6.5	5.0	0.1	1.0	1.0	0.1	0.1	0.5	45°	0.9884	2.5395	1.1921
0.3	0.1	6.5	5.0	0.1	1.0	1.0	0.1	0.1	0.5	45°	0.6511	2.5684	1.1927
0.1	0.3	6.5	5.0	0.1	1.0	1.0	0.1	0.1	0.5	45°	0.6916	2.5810	1.1757
0.1	0.1	10.0	5.0	0.1	1.0	1.0	0.1	0.1	0.5	45°	1.1002	2.5403	1.1926
0.1	0.1	6.5	10.0	0.1	1.0	1.0	0.1	0.1	0.5	45°	0.7970	3.1801	1.1930
0.1	0.1	6.5	5.0	0.5	1.0	1.0	0.1	0.1	0.5	45°	0.8835	2.5411	1.2113
0.1	0.1	6.5	5.0	0.1	3.0	1.0	0.1	0.1	0.5	45°	1.1188	2.5531	1.2193
0.1	0.1	6.5	5.0	0.1	1.0	0.5	0.1	0.1	0.5	45°	0.5908	2.5555	1.1675
0.1	0.1	6.5	5.0	0.1	1.0	1.0	0.5	0.1	0.5	45°	0.9930	2.5491	1.0894
0.1	0.1	6.5	5.0	0.1	1.0	1.0	0.1	1.0	0.5	45°	0.9951	2.5538	1.1230
0.1	0.1	6.5	5.0	0.1	1.0	1.0	0.1	0.1	1.5	45°	1.0413	2.6750	1.7531
0.1	0.1	6.5	5.0	0.1	1.0	1.0	0.1	0.1	0.5	60°	0.9278	2.5280	1.2057

Graphically Analysis

Velocity profile

For more information on how the magnetic field (M) affects the velocity outline for $\gamma < 1$ and $\gamma > 1$, refer to Figure 4.1. It designates that as the magnetic field intensity is increased, $f'(\eta)$ (a dimensionless velocity profile) decreases for $\gamma < 1$ and grows for $\gamma > 1$. Furthermore, for both $\gamma < 1$ and $\gamma > 1$, as illustrated in Figure 4.2, $f'(\eta)$

improves with the development of γ . Due to the formation of a boundary layer in the flow when $\gamma > 1$, or the free stream velocity, exceeds the stretching velocity, this is the case. Physically, the fluid motion rises close to the stagnation point, which causes the external stream's acceleration to rise. In turn, the thickness of the boundary layer decreases as γ increases. On the other hand, a reversed boundary layer forms when the stream velocity is smaller

than the stretching velocity, or $\gamma < 1$. When $\gamma = 1$, however, both velocities are equal and no boundary layer forms.

Temperature profile

Figure 4.3 shows how the temperature profile behaves when compared to the radiation parameter N. The temperature profile rises as the radiation parameter improves; the flow field generates heat as a result, increasing the temperature of the thermal boundary layer. See Figure 4.4 for the Brownian motion factor's impact on the temperature profile created for $\gamma < 1$ and $\gamma > 1$ values. Due to Brownian motion (Nb), which is the particles' erratic motion, the temperature profile rises in response to increasing values of (Nb), as the boundary layer warms up and the fluid temperature rises as a result. Explains the thermophoretic effects on the temperature profile against $\gamma < 1$ and $\gamma > 1$. Because changes in the wall and reference temperatures had a positive impact on the advancement of the thermophoretic

factor, the thermophoresis effect exhibits a direct relationship with the temperature field. how a rise in Pr causes a fall in temperature and a corresponding decrease in boundary layer thickness. Physically speaking, the larger Pr indicates that the momentum diffusivity is greater than the thermal diffusivity. The temperature decreased as a result of the decrease in thermal diffusivity.

Concentration profile

By taking $\gamma < 1$ and $\gamma > 1$ into account, Figure 4.5 describes the thermophoretic effect on $\phi(\eta)$. From the sketch, it can be inferred that the concentration is reduced for changed values of Nt. The concentration profile is decreased as a result of the boundary layer's thickness decreasing due to an increase in Nb against $\gamma < 1$ and $\gamma > 1$ (see Figure 4.6). Figure 4.7 demonstrates how the concentration profile drops off as Le increases. The Lewis number decreases the thickness of the boundary layer.

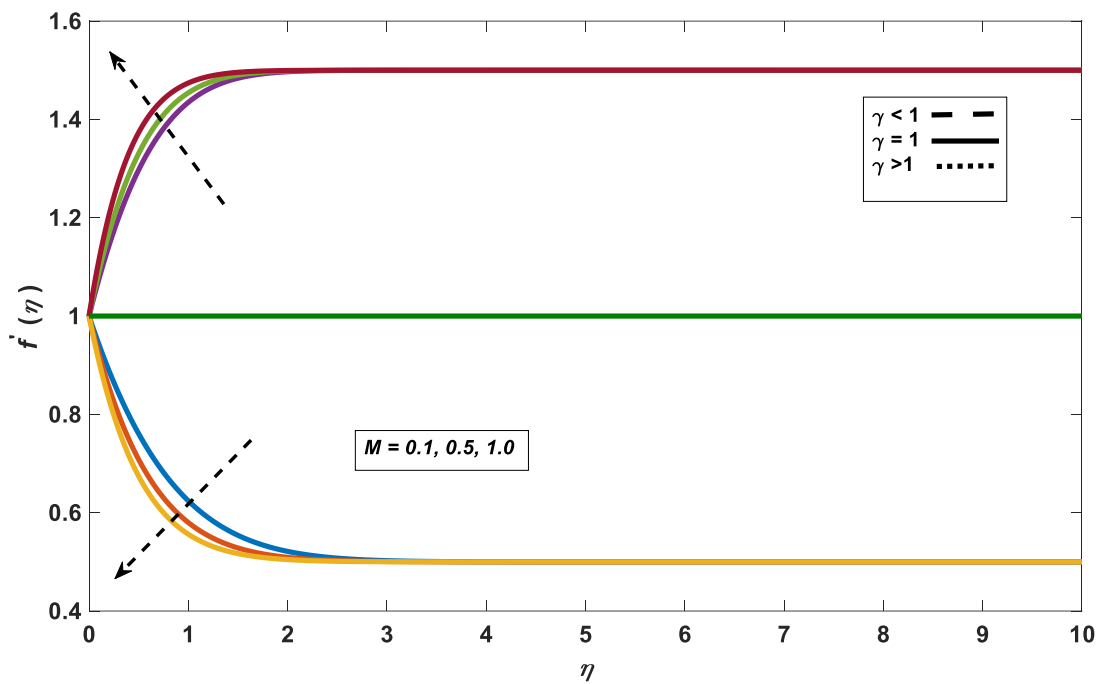


Fig.4.1. Impacts of Magnetic parameter (M) on f' (eta).

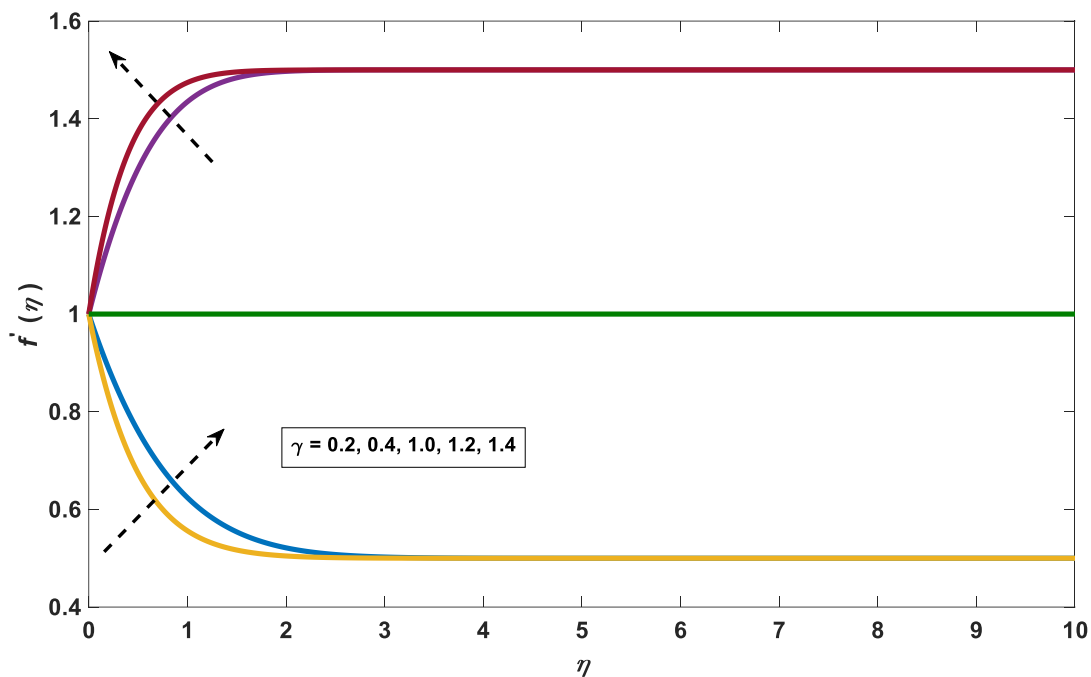


Fig.4.2. Impacts of Buoyancy parameter (λ) on $f'(\eta)$.

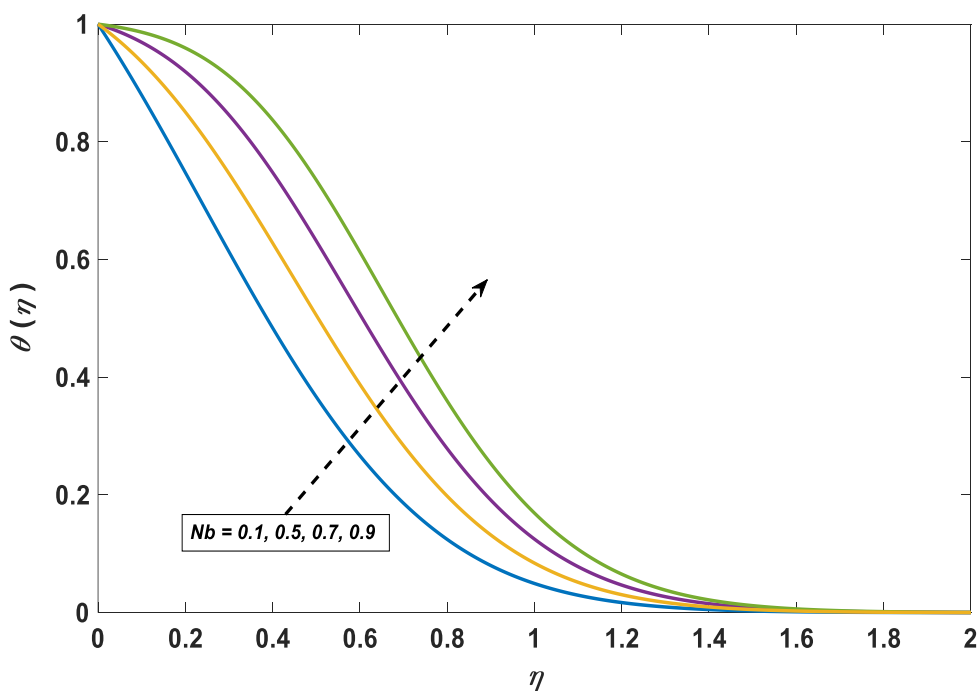


Fig.4.3. Impacts of Brownian motion parameter (Nb) on $\theta(\eta)$.

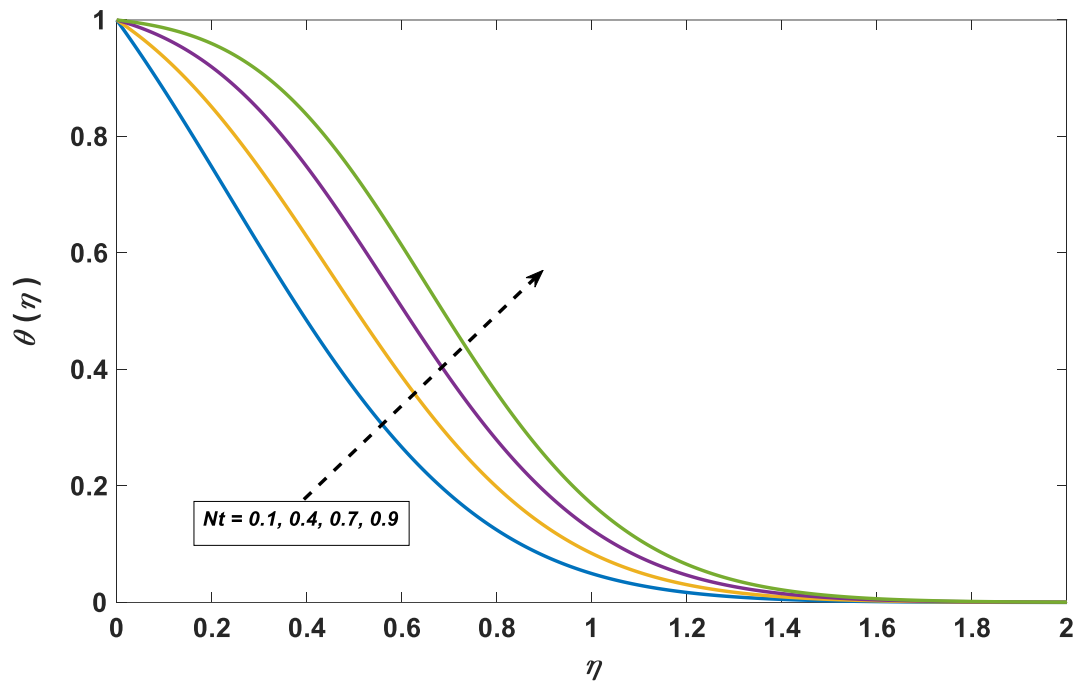


Fig.4.4. Impacts of Thermophoresis parameter (Nt) on (η) .

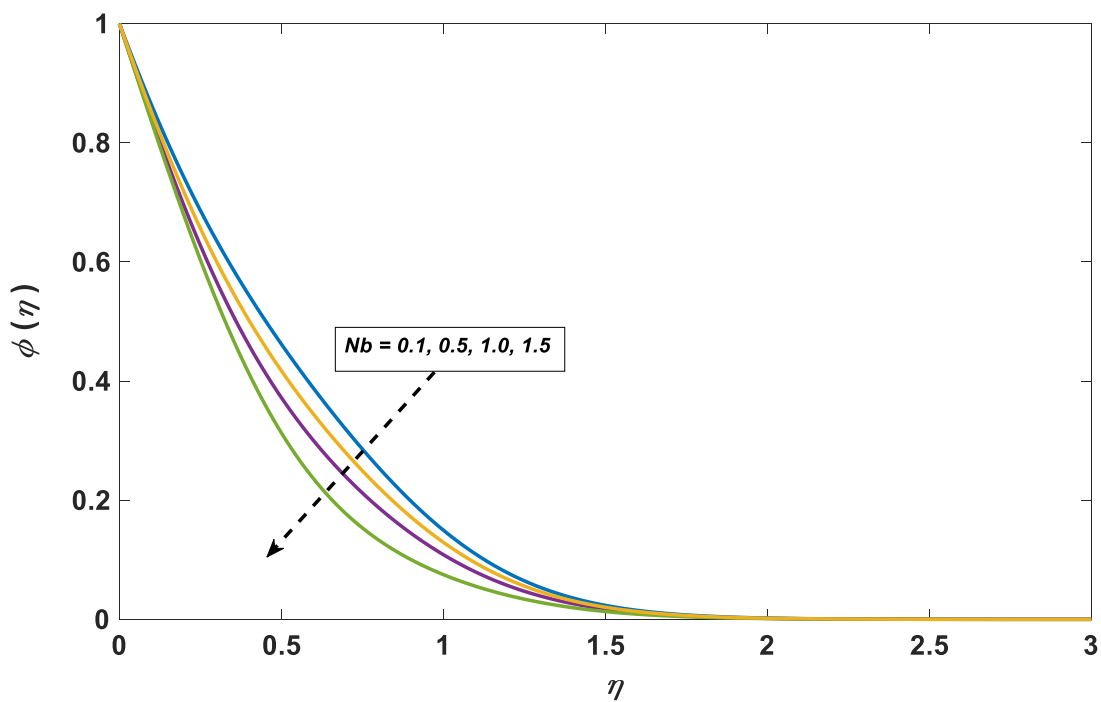


Fig.4.5. Impacts of Brownian motion parameter (Nb) on $\phi(\eta)$.

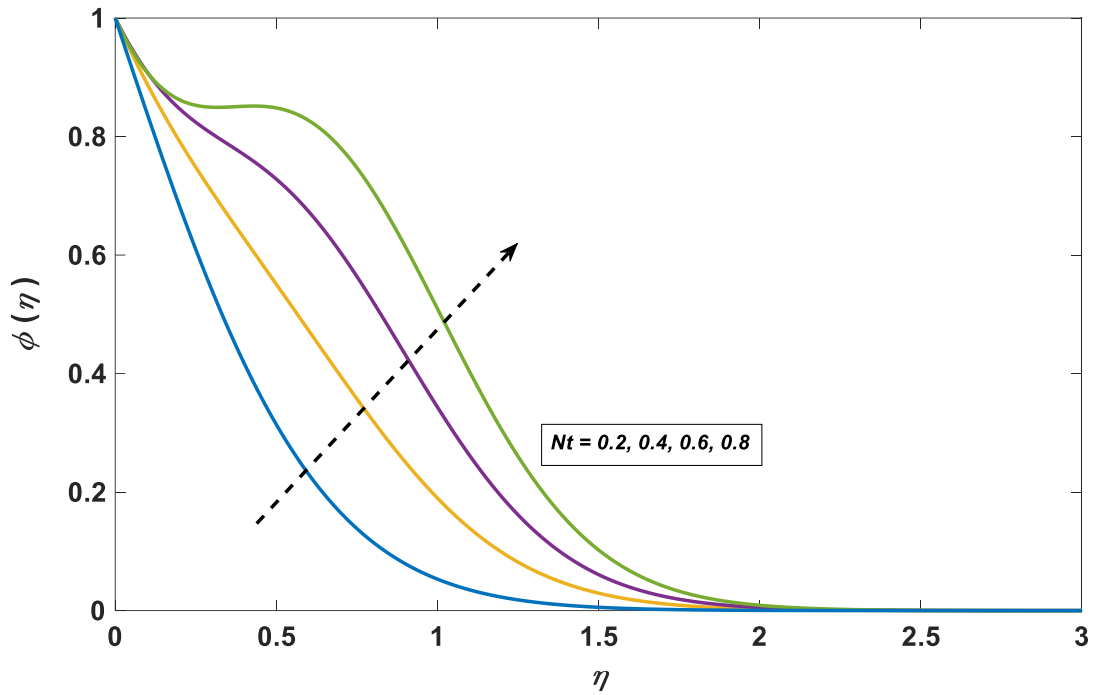


Fig.4.6. Impacts of Thermophoresis parameter (Nt) on $\phi(\eta)$.

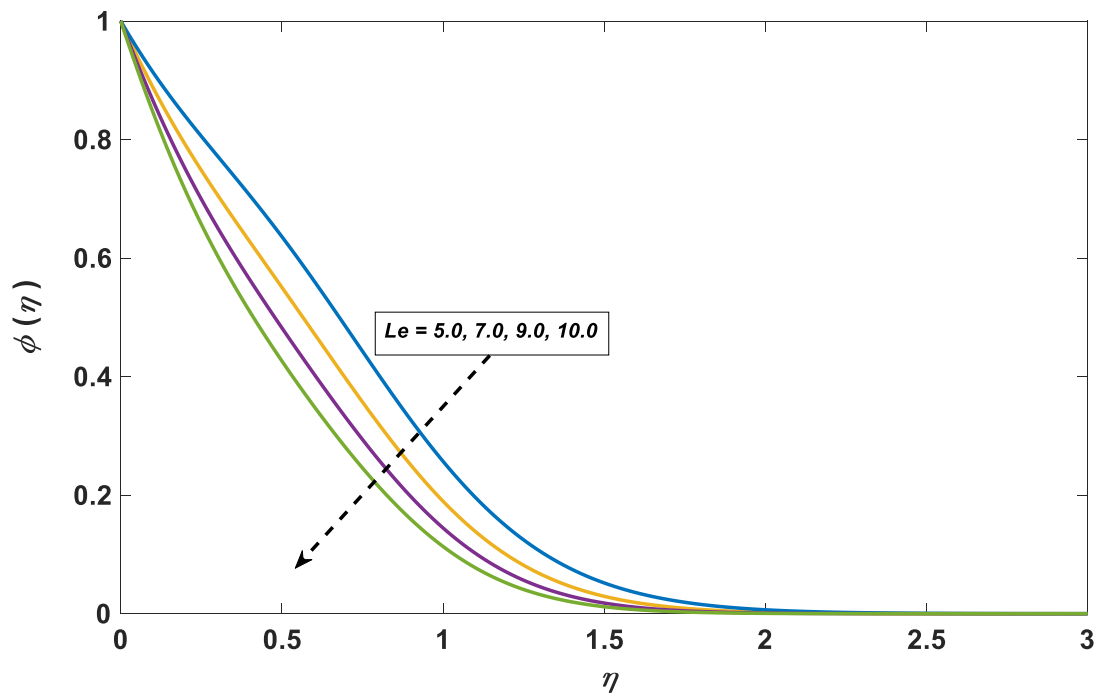


Fig.4.7. Impacts of Lewis number (Le) on (η) .

V. CONCLUSION

In the current study, the stagnation-point flow of a Casson nanofluid towards a stretched sheet is numerically explored by using magnetohydrodynamic (MHD) theory. The impacts of the Le , Nt , M , Nb , β , Pr , and the velocity ratio parameter γ are included in the model of nanofluid.

Mathematical equations are converted to nonlinear ODE. Then, we using a common numerical technique known as the Keller-Box technique, mathematically solved transformed equations. After that, analyze the problem with tabular and graphic data. Concentration profile,

temperature, velocity, Sherwood number, and are all employed for various flow parameters.

The numerical results are established using Bidin and Nazar (2009) and Ishak (2011), previously published work and a respectable settlement is acknowledged. The following are the key findings of this research:

- when Nb, N, Nt, M and ω are increased, $\theta'(0)$ lowers, whereas $Pr, \gamma, \lambda, \beta$, and δ are increased, $\theta'(0)$ grows.
- $-\theta'(0)$ is decreasing while rising ω and M . While, rising with higher values of $\beta, \delta, \gamma, \lambda, Pr, Nt, N, Nb$, and Le .
- $C_{fx}(0)$ decreases as Nt, λ, N and δ increases, when Nb, Le, β, M, ω and Pr increases values rise.
- $-\theta'(0)$ increases for increasing values of (N) while $-\theta'(0)$ and $C_{fx}(0)$ decreases.
- $C_{fx}(0)$ increases as the inclination factor (ω) increases, but $-\theta'(0)$ and $-\theta'(0)$ decreases.

REFERENCES

- [1] Al-Kouz, W. &. ((2022)). Numerical analysis of Casson nanofluid three-dimensional flow over a rotating frame exposed to a prescribed heat flux with viscous heating. *Scientific Reports*, 12(1), 1-17
- [2] Abd El-Aziz, M., & Afify, A. A. (2019). MHD Casson fluid flow over a stretching sheet with entropy generation analysis and Hall influence. *Entropy*, 21(6), 592..
- [3] Almakki, M., Mondal, H., & Sibanda, P. (2021). Onset of unsteady MHD Micropolar nanofluid flow with entropy generation. *International Journal of Ambient Energy*, 1-14.
- [4] Al-Mamun, A., Arifuzzaman, S. M., Alam, U. S., Islam, S., & Khan, M. (2021). Numerical simulation of periodic MHD casson nanofluid flow through porous stretching sheet. *SN Applied Sciences*, 3(2), 1-14.
- [5] Alsaadi, F. E., Ullah, I., Hayat, T., & Alsaadi, F. E. (2020). Entropy generation in nonlinear mixed convective flow of nanofluid in porous space influenced by Arrhenius activation energy and thermal radiation. *Journal of Thermal Analysis and Calorimetry*, 140(2), 799-809.
- [6] Anderson, J. D. (2005). Ludwig Prandtl's boundary layer. *Physics today*, 58(12), 42-48.
- [7] Atif, S. M., Kamran, A., & Shah, S. (2021). MHD micropolar nanofluid with non Fourier and non Fick's law. *International Communications in Heat and Mass Transfer*, 122, 105114.
- [8] Awais, M., Raja, M. A. Z., Awan, S. E., Shoaib, M., & Ali, H. M. (2021). Heat and mass transfer phenomenon for the dynamics of Casson fluid through porous medium over shrinking wall subject to Lorentz force and heat source/sink. *Alexandria Engineering Journal*, 60(1), 1355-1363.
- [9] Alwawi, F. A. (2020). MHD natural convection of Sodium Alginate Casson nanofluid over a solid sphere. *Results in physics*, 16, 102818.
- [10] Alwawi, F. A. (2020). Heat transfer analysis of ethylene glycol-based Casson nanofluid around a horizontal circular cylinder with MHD effect. *Proceedings of the Institution of Mechanical Engineers*, journal of mechanical engineering, 2569-2580.
- [11] Bhattacharyya, K. (2013). MHD stagnation-point flow of Casson fluid and heat transfer over a stretching sheet with thermal radiation. *Journal of thermodynamics*, 2013.
- [12] Chand, R., Yadav, D., Bhattacharyya, K., & Awasthi, M. K. (2021). Thermal convection in a layer of micropolar nanofluid. *Asia-Pacific Journal of Chemical Engineering*, 16(5), e2681.
- [13] Cui, W., Cao, Z., Li, X., Lu, L., Ma, T., & Wang, Q. (2022). Experimental investigation and artificial intelligent estimation of thermal conductivity of nanofluids with different nanoparticles shapes. *Powder Technology*, 398, 117078.
- [14] Cui, X., Wang, J., & Xia, G. (2022). Enhanced thermal conductivity of nanofluids by introducing Janus particles. *Nanoscale*, 14(1), 99-107.
- [15] Esfe, M. H., Kamyab, M. H., & Toghraie, D. (2022). Statistical review of studies on the estimation of thermophysical properties of nanofluids using artificial neural network (ANN). *Powder Technology*, 117210.
- [16] Fatunmbi, E. O., & Salawu, S. O. (2022). Analysis of hydromagnetic micropolar nanofluid flow past a nonlinear stretchable sheet and entropy generation with Navier slips. *International Journal of Modelling and Simulation*, 42(3), 359-369.
- [17] Gbadeyan, J. A. (2020). Effect of variable thermal conductivity and viscosity on Casson nanofluid flow with convective heating and velocity slip. *Heliyon*, 6(1), e03076.
- [18] Hayat, T., Ullah, I., Waqas, M., & Alsaedi, A. (2018). MHD stratified nanofluid flow by slandering surface. *Physica Scripta*, 93(11), 115701.
- [19] Hussain, T., & Xu, H. (2022). Time-dependent squeezing bio-thermal MHD convection flow of a micropolar nanofluid between two parallel disks with multiple slip effects. *Case Studies in Thermal Engineering*, 31, 101850.
- [20] Jamshed, W. K. (2022). Computational examination of Casson nanofluid due to a non-linear stretching sheet subjected to particle shape factor: Tiwari and Das model. *Numerical Methods for Partial Differential Equations*, 848-875
- [21] Jamshed, W. K. (2022). Computational examination of Casson nanofluid due to a non-linear stretching sheet subjected to particle shape factor: Tiwari and Das model. *Numerical Methods for Partial Differential Equations*, 848-875.
- [22] Khan, K. A., Jamil, F., Ali, J., Khan, I., Ahmed, N., Andualem, M., & Rafiq, M. (2022). Analytical simulation of heat and mass transmission in casson fluid flow across a stretching surface. *Mathematical Problems in Engineering*, 2022.
- [23] Khan, S. U., Bhatti, M. M., & Riaz, A. (2020). A revised viscoelastic micropolar nanofluid model with motile micro-organisms and variable thermal conductivity. *Heat Transfer*, 49(6), 3726-3741.

- [24] Khan, W.A. and Pop, I. (2010) Boundary-Layer Flow of a Nanofluid past a Stretching Sheet. *International Journal of Heat and Mass Transfer*, 53, 2477-2483.
- [25] Lund, L. A., Omar, Z., Khan, U., Khan, I., Baleanu, D., & Nisar, K. S. (2020). Stability analysis and dual solutions of micropolar nanofluid over the inclined stretching/shrinking surface with convective boundary condition. *Symmetry*, 12(1), 74.
- [26] Mabood, F., & Das, K. (2019). Outlining the impact of melting on MHD Casson fluid flow past a stretching sheet in a porous medium with radiation. *Heliyon*, 5(2), e01216.
- [27] Mehta, B., & Subhedar, D. (2022). Review on mechanism and parameters affecting thermal conductivity of nanofluid. *Materials Today: Proceedings*, 56, 2031-2037.
- [28] Mustafa, M., Hayat, T., Ioan, P., & Hendi, A. (2012). Stagnation-point flow and heat transfer of a Casson fluid towards a stretching sheet. *Zeitschrift für Naturforschung A*, 67(1-2), 70-76.
- [29] Porous stretching surface in presence of thermal radiation. *Ain Shams Engineering Journal*, 5(1), 205-212. Pramanik, S. (2014). Casson fluid flow and heat transfer past an exponentially.
- [30] Rafique, K., Alotaibi, H., Ibrar, N., & Khan, I. (2022). Stratified Flow of Micropolar Nanofluid over Riga Plate: Numerical Analysis. *Energies*, 15(1), 316.
- [31] Rafique, K., Anwar, M. I., & Misiran, M. (2019). Keller-box study on casson nano fluid flow over a slanted permeable surface with chemical reaction. *Asian Res. J. Math*, 14, 1-17.
- [32] Rafique, K., Anwar, M. I., Misiran, M., Khan, I., Alharbi, S. O., Thounthong, P., & Nisar, K. S. (2019). Numerical solution of casson nanofluid flow over a non-linear inclined surface with soret and dufour effects by keller-box method. *Frontiers in Physics*, 7, 139.
- [33] Rafique, K., Imran Anwar, M., Misiran, M., Khan, I., Alharbi, S. O., Thounthong, P., & Nisar, K. S. (2019). Keller-box analysis of Buongiorno model with Brownian and thermophoretic diffusion for Casson nanofluid over an inclined surface. *Symmetry*, 11(11), 1370.
- [34] Ramesh, G. K., Roopa, G. S., Rauf, A., Shehzad, S. A., & Abbasi, F. M. (2021). Time-dependent squeezing flow of Casson-micropolar nanofluid with injection/suction and slip effects. *International Communications in Heat and Mass Transfer*, 126, 105470.
- [35] Rehman, K. U., Khan, A. U., Rehman, F., & Shatanawi, W. (2022). Thermal case study on linearly twisting cylinder: a radial stagnation point flow of nanofluid. *Case Studies in Thermal Engineering*, 31, 101861.
- [36] Sakiadis, B. C. (1961). Boundary-layer behavior on continuous solid surfaces: II. The boundary layer on a continuous flat surface. *AiChE journal*, 7(2), 221-225.
- [37] Tayebi, T., Dogonchi, A. S., Chamkha, A. J., Hamida, M. B. B., El-Sapa, S., & Galal, A. M. (2022). Micropolar nanofluid thermal free convection and entropy generation through an inclined I-shaped enclosure with two hot cylinders. *Case Studies in Thermal Engineering*, 101813.
- [38] Uddin, I., Ullah, I., Raja, M. A. Z., Shoaib, M., Islam, S., & Muhammad, T. (2021). Design of intelligent computing networks for numerical treatment of thin film flow of Maxwell nanofluid over a stretched and rotating surface. *Surfaces and Interfaces*, 24, 101107.
- [39] Xu, H., Chang, C., Zhang, J., Xu, J., Chen, H., Guo, H., ... & Deng, T. (2022). Transparent nanofluids with high thermal conductivity for improved convective thermal management of optoelectronic devices. *Experimental Heat Transfer*, 35(2), 183-195.

Reuse of Greywater and its Role in the Sustainability of Water Resources – A Study in Saudi Arabia

Anbarah Khamis B. Al-Saud

Department of Geography, College of Humanities and Social Sciences, King Saud University, Kingdom of Saudi Arabia

<https://orcid.org/0000-0003-3199-5074>

Email: aassaod@ksu.edu.sa

Received: 08 Feb 2024,

Receive in revised form: 19 Mar 2024,

Accepted: 05 Apr 2024,

Available online: 14 Apr 2024

©2024 The Author(s). Published by AI
Publication. This is an open access article under
the CC BY license

(<https://creativecommons.org/licenses/by/4.0/>)

Keywords— Reuse of greywater, natural characteristics, lack of potable water, BOD, COD, Saudi Arabia.

Abstract— Reuse of greywater has become one of the proposed solutions worldwide to support water resources; that are subject to depletion in desert areas such as Saudi Arabia, where rainfall is scarce, suffering growing water demand for municipal and agricultural purposes, and the sustainability of groundwater resources on the other. In Saudi Arabia greywater represents nearly 55-74% of the water consumed in the buildings; so this study aimed to answer the following question: According to ministerial order No. 228 of 29 August 1426 AH, which stipulates that greywater should be reused and that two wastewater recycling systems should be implemented in the development of specifications and plans for the construction of new installations in the sectors concerned; Are there any indicators which prove the implementation of this ministerial decision? What is the evidence for this application? The reuse of treated greywater depends on the natural, chemical, and physical characteristics of the amount of biological consumption of oxygen (BOD5), total suspended solids (TSS), and the chemical oxygen demand (COD). The study concluded that some of the general natural characteristics of water are similar in value to those of high-income and low-income countries. The results show a continuous increase in water consumed through the study period within the urban and agricultural sectors, of Saudi Arabia into global support for the conservation of natural resources.

I. INTRODUCTION

Daily demand for freshwater in the civil, industrial, agricultural, and other sectors increases yearly. This demand corresponds to many factors such as the annual growth of the world's population, on the one hand, and to the disparity in their living standards, on the other [1]. These are the key variables that explain the annual increase in the amount of clean water consumed worldwide. On-demand for clean water: More than three billion people are expected to live by 2025 under the current 0.8 billion water stress threshold conditions [2]. They also pointed out that globally, the total volume of directly exploitable

freshwater is only 1/100 of 3% of complete freshwater resources, which is well below the total human demand (Ibid). Of course, the percentage of greywater discharged from the residential sector varies at the regional level. The reason for this discrepancy depends on the primary use of water in the dwellings and the efficiency of the service of such water [3]. The reuse of treated water is mentioned in many kinds of literature and was advised by many global environmental agencies, including the United States Environmental Protection Agency EPA [4], to gain the ecological dimension of the sustainable development goals. Reusing greywater has recently become an essential strategic solution to secure water scarcity in Saudi Arabia's

agricultural and industrial sectors [5]. Alternative water management strategies have been set up in dry territories because of the absence of freshwater [6]. This consecutive demand for fresh was associated with some geographical locations such as Saudi Arabia, Scarcity of supply of such water for different geographical reasons, Extremism in prevailing climatic conditions and its impact on the scarcity and occasional scarcity of rainfall, as in the desert regions, or one of the reasons for this scarcity may be poor consumption or mismanagement of available water resources. No doubt: It was accompanied by increased water consumption in various areas, an Increase in the amount of water used, and discharge to the public sewerage network [7]. Greywater was defined as water used by the State to meet the continuing demand for it for various civilian purposes, for example, in the residential sector for multiple purposes including bathing, washing clothes, kitchen, etc. [8]. There is also a similar definition of greywater: "Greywater is defined as a domestic wastewater that is uncontaminated by direct contact with human excreta [9]. Greywater was defined as water used for washing machines, baths, kitchen laundry, and laundry [10],[11], and greywater is any household wastewater produced except for sewage or black water [12]. "Reuse of treated greywater has become a demand, especially in those countries with natural and economic challenges in accessing safe water." The proportion of greywater discharged from the residential sector is up to 75% [13]. In Jordan, it is between 50 and 80% of the sewage for the residential sector ([14]. Since there is a rise in water use, the amount of wastewater discharged into public sewage systems is expected to increase. Thus, at the outset, it must be considered that greywater is one of the main sections of wastewater [15]. Some believe that greywater discharged from the residential sector, such as bathing water, and without purification, can be used for certain uses, such as irrigating crops in comparison to black water [16]. Of course, As the demand for water increases in various sectors in any of them, so does the amount of greywater. The relationship between the amount of demand for clean water and the amount of used water discharged is an evolutionary one. What's bad is that the increase in the amount of greywater that will undoubtedly flow into the public sewage system if it's not treated before, so that it becomes reusable in the sectors that consume it. Globally, it's estimated that 50-80% of sewage comes from greywater (Aljaysosi, op.cit.) explained that a case study was presented on the reuse of greywater in Jordan to shed some light on its role in sustainable water management. To operationalize this concept, water is seen as an economic commodity and a limited resource that should be evaluated and managed rationally. Notwithstanding the importance

of the reuse of greywater in alleviating the demand for freshwater sources and protecting them from depletion; this is not without the technical and economic challenges that societies in low-income countries will face. Statistical data shows that the percentage of wastewater from the residential sector treated safely varied globally between developing and developed countries; and between countries with higher and lower incomes in 2020 (figure 1). Many countries were green color, which means a high percentage of safely treated wastewater flows from households. The darkest green color means > 90% as in the United States, France, Japan, Sewed, Finland, and other countries with high economies. Otherwise, the rest of the countries which appeared in a disparity of light green color, including Saudi Arabia, Algeria, Norway, Spain, Australia, New Zealand, Turkey, and other countries with the same rates of treatment are under 90% and up by 25%. The important notice matter wasn't in the groups of countries with other colors; but in the rest of the countries that appeared in grey color as no data, and the more dangerous thing of the countries which not yet begun the reuse of greywater, and both of that two groups classified of low economy and poor countries.

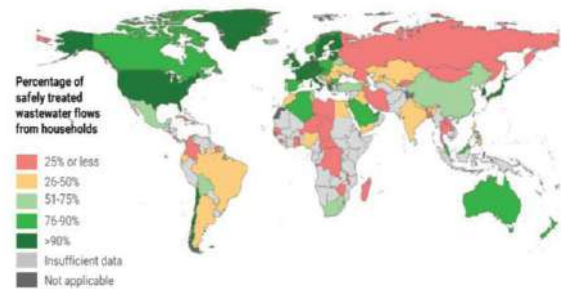


Fig.1: Estimated proportions wastewater safely treated (2020), Source: [17].

Using treated greywater is expected to reduce the demand for freshwater use within residential, governmental, and service sectors. If specific treatment policies are implemented, the greywater will be recycled to meet the increasing demand. When deciding to treat greywater for reuse, it should be known that this water differs in terms of whether it is a high load or low load, as shown in (Figure 2); Water discharged from hand-washing and fast bathing basins is classified as "light water," while water discharged from the kitchen basin and dishwasher is "heavy water." In Saudi Arabia the greywater removed from the washbasins in mosques is the purest compared to the previous greywater sources. It, therefore, requires only simple and economically inexpensive purification (General Administration of Sanitation, op.cit.)

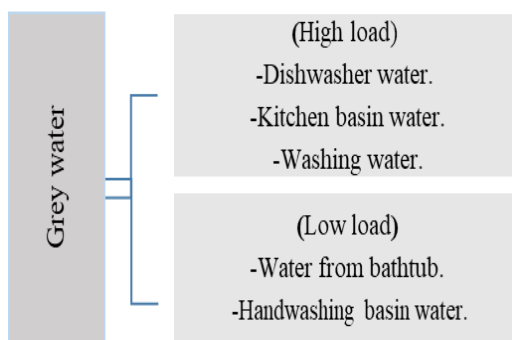


Fig.2: Classification of greywater by payload.

Source: this diagram was designed by the researcher.

Although the process of greywater reuse includes several natural, economic, and social benefits in the sense that it would achieve the globally recognized triad of sustainable development; the success of this operation depends on the type of pollutants that may be present in such water, according to sources (Allen, op.cit). BOD5 is the acronym for Biochemical Oxygen Demand and is widely used for cxin biological wastewater treatment. It is known as a standardized unit for measuring organic water pollution. Through BOD5, the mass of molecular oxygen consumed by micro-organisms in five days in one Liter of water at 20°C in the dark [18].

In a country such as Saudi Arabia, which is within the arid tropical desert climate region, the attendant scarcity and sudden rainfall on its territory, which, although covering a land area of approximately 2 million km², is devoid of permanent inland water bodies, such as lakes, rivers, and waterfalls. Otherwise, temporary waterways, such as the stream of valleys, appear after the winter rains in all areas of the Kingdom of Saudi Arabia and after the summer rains fall exclusively on the mountain's lands of the southwest of the Kingdom of Saudi Arabia.

II. STUDY AREA

Saudi Arabia lies between 16° and 32° north of the equator (Figure 3). As a result of the astronomical nature of this site, extreme climatic characteristics prevail throughout the year. The study area has no permanent water bodies, such as lakes or rivers. Apart from this, there are hundreds of dry valleys in which water flows at varying intervals immediately after the rains fall. Meeting the increasing water demand depends on several traditional sources, namely deep and surface groundwater, and salt-water desalination plants, located directly to the Red Sea and Arabian Gulf. The decision-makers valued the importance of preserving groundwater, therefore, issued ministerial order No. 228 of 29 August 1426AH. Under

the terms of the Act on the Reuse of Greywater, two water-recycling systems must be implemented in the formulation of specifications and plans for the construction of new installations in the sectors [19], as well as the promulgation of several programs and initiatives dealing with freshwater consumption regulations; however, with the successive annual increase in the population of the Kingdom of Saudi Arabia, which reached 32,175,224 people in 2022 [20]. Hence, the increased demand for water for the agricultural sector, which meets the requirements of producing various plant and animal foods, increases the amount of greywater discharged from farming and other sectors.

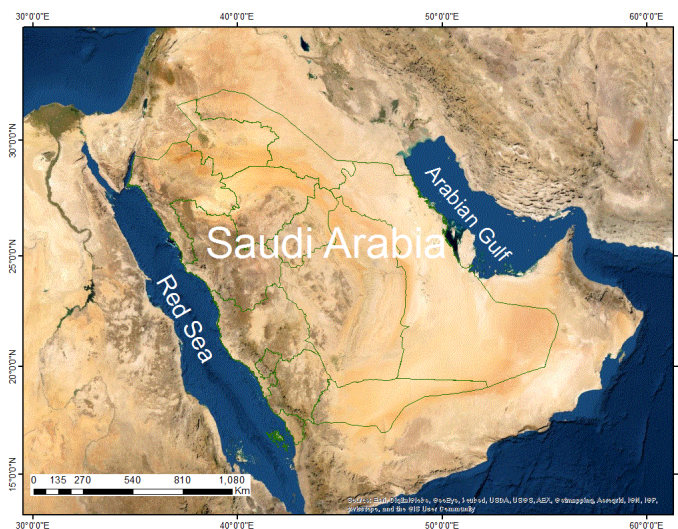


Fig.3: Map of the study area

Source: the researcher.

III. METHODOLOGY

Statistical data of freshwater consumption in the municipal, industrial, and agricultural sectors, other data on the source of that freshwater, as well as data on the amount of wastewater, and the amount of what was treated during the study period 2009-2020 in the Kingdom of Saudi Arabia; that issued in the statistical yearbook, and the annual reports of the Ministry of Environment, Water, and Agriculture. Information was also collected from the statistical yearbook of the General Authority for Statistics. Graphs were drawn that showed the nature of freshwater consumption within the urban and agricultural sectors and the change in the amount of treated water reused during the study period.

IV. ANALYSIS AND DISCUSSION

Tracking freshwater demand in any population area proves to be subject to constant change. The quantity of

freshwater demand in the Kingdom of Saudi Arabia changed during the study period 2010-2020, as this demand increased from 17447 million m³ in 2010 to 25992 million m³ in 2018. In 2019, the consumption decreased significantly to 15393 million m³, but it increased slightly to 15979 million m³ in 2020 Table (1). It noted that just as there was a variation in the amount of water demand during the study period, the data in the same Table also shows a disparity in the amount of water consumption within the three municipal, industrial, and agricultural sectors. Water consumption within the municipal sector, as well as the industrial sector, has been characterized by continuous increases. Data in Table (1) shows that the volume of water consumption within the municipal sector increased from 2.2 million m³ in 2010 to 3.6 million m³ in 2020. This leading sector includes all sub-sectors, mainly residential, health, educational, and services. This increase reflects the impact of key variables within these sectors. The growth in population size and the consequent diverse water requirements play primarily within the residential sector, which includes drinking, cooking, bathing, washing clothes and kitchen utensils, as well as other uses such as garden irrigation and yard washing. The percentage of water demand in the urban sector reached 23% in 2020. Although water consumption in the industrial sector was characterized by a continuous increase during the years of study from 753 million m³ to 1680 million m³, this amount represented only 10% of the total amount of water demand in the Kingdom of Saudi Arabia in 2020. Finally, the water demand reached the highest in the agricultural sector, becoming the dominant sector in the total water demand during the study period by 82.5% in 2010 and 66.7% in 2020. The percentage of this dominance over the total amount of water consumption during the study period was 82.5% in 2010 and 81.5% in 2018 (Table 1). The decline in the amount of water demand in the agricultural sector (Figure 4) and (Figure 5) reflects the efforts of the Ministry of Environment, Water and Resources to adopt the water demand management approach and not meet it to keep pace with the global trend in this important matter [21]. By applying this policy, Saudi Arabia engages the global a crucial role in sustaining its rare water resource.

Table 1: Amount of freshwater consumption 2010-2020 (million m³/year)

	2010	2012	2014	2016	2018	2020
Municipal	2284	2527	2874	3130	3428	3629
Industrial	573	843	930	1015	1400	1680

Agricultural	1441	1751	1961	1978	1900	1067
(non-renewable water)	0	4	2	9	0	0
Total	1726	2088	2341	2393	2382	1597
	7	4	6	4	8	9
% For consumption of the agricultural sector	83.4	83.8	83.7	82.6	79.7	66.7

Source: Ministry of Environment, Water and Agriculture (2020). Statistical Yearbook: 1441-1442 AH.

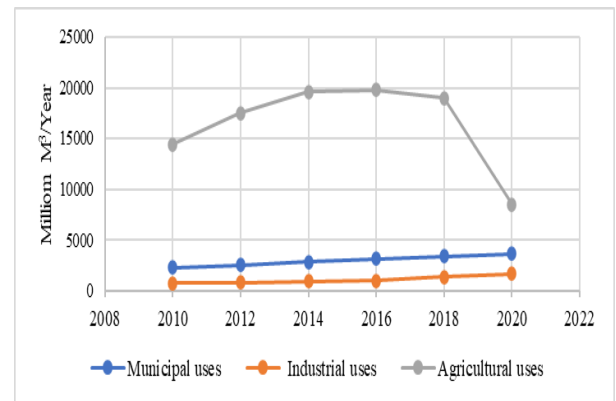


Fig.4 Sectoral distribution of freshwater consumed in Source: prepared by the researcher.

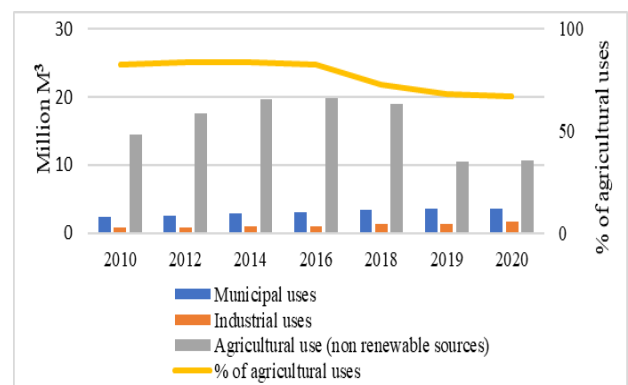


Fig.5: Amount of freshwater consumption in all sectors from 2010 to 2020 (million m³/year). Source: prepared by the researcher.

Conventional and non-conventional sources have played essential roles in meeting the growing annual demand for water in the municipal, agricultural, and industrial sectors. Data collected from the General Authority for Statistics

showed that the non-renewable groundwater sector is the primary source of the freshwater demand, as it plays an important role compared to other sources in terms of the amount of water it provides to meet the increasing domestic demand for fresh water from various sectors during the study period (Figure 6).

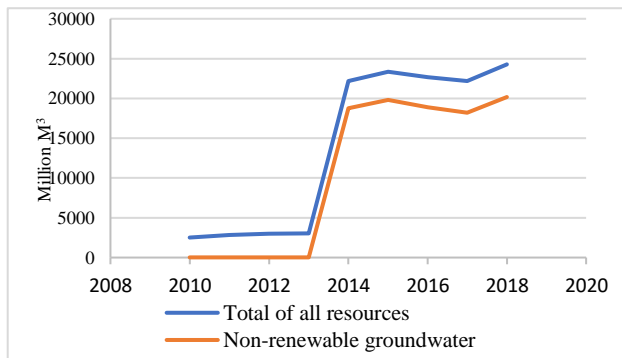


Fig.6: The predominance of non-renewable groundwater over total. Source: The researcher.

Due to the scarcity of rainfall at times and the limited amount of rain at other times due to the nature of the prevailing climate, which is the direct source that feeds surface and deep groundwater, and due to the continuously increasing demand for freshwater, the attention of decision-makers has once again focused on the reuse of greywater. Every increase in clean water consumption will be offset by an increase in the amount of greywater discharged into sewage channels, so the greywater reuse initiative has been activated.

Data in (Table 2) show that government decisions have played a crucial role in dealing with wastewater in a more beneficial way that ensures the sustainability of groundwater resources. What is noticeable about these data are two things: the growth of the quantities of that treated water, and finally, the % reused water quantity of the total processed fluid through the years from 2018 to 2020. There are many advantages of reusing greywater; one represented 55-74% of the water used in building. It is also easy to deal with the low pollution from organic matter, nitrogen, germs, and microbes during purification stages (Ministry of Environment Water and Agriculture, op. cit). The process of reusing treated water for living requirements depends on crucial things, the first of which is acceptance from members of society. Otherwise, the reuse of greywater is such a sensitive thing. The reuse of treated greywater depends on the natural, chemical, and biological characteristics of the amount of physical consumption of oxygen (BOD5), total suspended solids (TSS), and the chemical oxygen demand (COD). The study concluded that only some of the general natural characteristics of water in Saudi Arabia are similar in

value to those of high-income and low-income countries (Table 3). The importance of greywater reuse in groundwater sustainability in the Kingdom of Saudi Arabia requires new analytical studies to fill in the gaps in some parameters of the characteristics mentioned in this table.

Table 2: quantities of treated wastewater

	Quantity of treated wastewater (M ³ /year)	Average amount of treated wastewater (M ³ /day)	Average amount of water reused (M ³ /day)	% of reused water quantity of the total processed fluid
2018	1665059190	4561806	862140	18.11
2019	1801873551	4936640	852307	17.26
2020	1868573838	5105431	929252	18.20

Source: Preparation by the researcher based on the Ministry of Agriculture, Water and Environment, Statistical Yearbook from 2018 to 2020

Table 3: Physicochemical characteristic of greywater s in low- and high-income countries

Parameter	Low-income countries ^a	High-income countries ^a	Saudi Arabia ^b
pH	6.7	7.17	-
Turbidity (NTU)	35.2	41.35	-
TSS (mg/L)	285.8	48.0	-
TDS (mg/L)	337.5	171.0	-
BOD5 (mg/L)	206.0	80.6	-
COD (mg/L)	819.5	204.8	-
TOC (mg/L)	-	-	-
Oil and grease (mg/L)	7.0	-	-
Nitrate (mg/L)	49.3	3.9	-

Source: Preparation by the researcher.

^a Peprah, Acheampong and deVries, 2018.

^b Ministry of Water and Electricity, General Department of Sanitation. Greywater Reuse Guide. Second edition, (1429h).

V. CONCLUSION

Reusing greywater is play an important role in sustaining water resources in the arid areas. The ability of using treated greywater depend on the Physicochemical characteristic BOD5, TOD, SST. Grow in freshwater consumption in dry areas will lead to an increase in continuous demand, and hence surface pressure and deep groundwater sources. Find other sources to support traditional water sources in these areas and adopt them as permanent sources to meet water demand, such as seawater desalination or reuse of greywater and wastewater after treatment. It is necessary to conduct applied analytical studies to reveal the values of the parameters of the natural characteristics of greywater in the study area to decide on its suitability for reuse, and to make the outputs of these research available for comparison with the results of international studies.

REFERENCES

- [1] Zadeh, S. M. Hunt, D.V.L. Lombardi, Rachel, D. and Rogers, D. F. R. and others. Carbon Costing for Mix-Use Greywater Recycling Systems. 2013
- [2] Ismaila Rimi Abubakar, Nuhu Dalhat Mu'azu, Household attitudes toward wastewater recycling in Saudi Arabia, Utilities Policy, Volume 76, 2022, 101372
- [3] Lucy Allen, Juliet Christian-Smith and Meena Palaniappan. Overview of Greywater Reuse: The Potential of Greywater Systems to Aid Sustainable Water Management. Pacific Institute, November 2010. ISBN: 1-893790-27-4
- [4] United States Environmental Protection Agency EPA. <https://www.epa.gov/waterreuse/basic-information-about-water-reuse#:~:text=Types%20of%20Water%20Reuse>
- [5] Alkhudhiri, A., Darwish, N.B., & Hilal, N. (2019). Analytical and forecasting study for wastewater treatment and water resources in Saudi Arabia. *Journal of Water Process Engineering*.
- [6] Shaikh, Samir & Shahapurkar, Rekha. (2021). Predicting COD and BOD Parameters of Greywater Using Multivariate Linear Regression. This article is published online with Open Access by IOS Press and distributed under the terms of the Creative Commons Attribution Non-Commercial License 4.0 (CC BY-NC 4.0). 10.3233/APC210199.
- [7] Murthy, P.M. Murthy, P.M., and Kavyas S. (2016). Greywater Treatment & Reuse: A Technological Review. *Global Journal for Research Analysis*. Vol. 5, Issue-3, March 2016. ISSN NO 2277-8160
<https://dictionary.cambridge.org/dictionary/english/grey-water>
- [8] A E Ghaly, N S Mahmoud, M M Ibrahim, E A Mostafa, E N Abdelrahman, R H Emam, M A, Kassem and M H Hatem (2021) Greywater Sources, Characteristics, Utilization and Management Guidelines. *Adn Envi Was Mana Rec*, 4 (2):128-145.
- [9] Albalawneh, A., & Chang, T. (2015). REVIEW OF THE GREYWATER AND PROPOSED GREYWATER RECYCLING SCHEME FOR AGRICULTURAL IRRIGATION REUSES.
<<https://www.ecomena.org/reuse-of-greywater>>.
- [10] (<https://www.sustainable.com.au/greywater-treatment>)
- [11] Oteng-Pepurah, M., Acheampong, M.A., & deVries, N.K. (2018). Greywater Characteristics, Treatment Systems, Reuse Strategies and User Perception—a Review. *Water, Air, and Soil Pollution*, 229. <https://doi.org/10.1007/s11270-018-3909-8>
- [12] Al-Jayyousi, Odeh. (2003). Greywater reuse: Towards sustainable water management. *Desalination*. 156. 181-192. 10.1016/S0011-9164(03)00340-0.
- [13] General Directorate of Sanitation, 1429H
- [14] Collins English Dictionary
- [15] Alabaster, Graham and Johnston, Richard (2021). *Progress on Wastewater Treatment. Global Status and Acceleration Needs for SDG Indicator 6.3.1*. United Nations and World Health Organization. ISBN 978-92-1-132878-3
- [16] <<https://www.learnandconnect.pollutec.com>>
- [17] -Ministry of Environment Water and Agriculture (1429). **Guidelines for Greywater Reuse**. 2nd edit.
- [18] General Statistics Authority, <<https://www.stats.gov.sa>>
- [19] Ministry of Environment, Water and Agriculture, (2020). Yearbook 1441-1442 A.H. 151 pages.

Design and Simulation of InGaAs/GaAsSb single quantum well structure for optical fiber application: Electronic Band Structure, Carrier Transport, and Optical Gain Analysis

Jayprakash Vijay

Department of Electronics and Communication, Swami Keshvanand Institute of Technology, Management & Gramothan, Jaipur, Rajasthan, India
E-Mail: jpvijay121@gmail.com

Received: 05 Feb 2024,

Receive in revised form: 20 Mar 2024,

Accepted: 01 Apr 2024,

Available online: 10 Apr 2024

©2024 The Author(s). Published by AI
Publication. This is an open access article under
the CC BY license

[\(https://creativecommons.org/licenses/by/4.0/\)](https://creativecommons.org/licenses/by/4.0/)

Keywords— *Quantum well structure, Optical gain, WDM/DWDM*

Abstract— *This paper explores the electronics and optical gain characteristics of an InGaAs/GaAsSb single quantum well structure designed on a GaAs substrate at room temperature (300 K). The findings indicate that this structure can emit radiation at 1550 nm with a significantly higher gain of approximately 6300/cm, rendering it suitable for optical fiber communication and optics applications such as WDM/DWDM for long-haul fiber transmission. This work contributes to advancing the field of optoelectronics by providing a promising solution for efficient NIR wavelength emission with substantial optical gain.*

I. INTRODUCTION

Optoelectronic devices utilizing compound semiconductors have revolutionized modern technology, enabling the development of high-performance systems for various applications, including telecommunications, data transmission, and sensing [1-3]. At the heart of these devices lies the intricate design of heterostructures, where different semiconductor materials with tailored properties are intricately combined to achieve specific functionalities [4]. The synergistic integration of various materials within heterostructures offers unparalleled opportunities to manipulate electronic and optical properties, paving the way for the creation of novel optoelectronic devices with enhanced performance characteristics. Compound semiconductors, such as InGaAs, GaAsSb, and related alloys, are particularly favored for optoelectronic applications due to their unique optical and electrical properties, including direct bandgaps, high electron mobilities, and compatibility with lattice-matched

substrates [5-9]. These materials serve as the building blocks for the construction of heterostructures, where precise control over layer thickness, composition, and doping profiles is crucial to tailor the device's optical and electronic properties. The design of heterostructures for optoelectronic devices involves intricate considerations, including band alignment engineering, carrier confinement, and optical gain optimization [10]. By judiciously selecting materials and layer configurations, researchers can tailor the band structure to achieve desired electronic and optical characteristics, such as efficient carrier transport, enhanced light-matter interaction, and high optical gain. Advanced simulation tools, such as density functional theory (DFT), empirical pseudopotential method (EPM), and finite element methods (FEM), play a crucial role in predicting and optimizing the performance of heterostructures prior to fabrication [11]. In this context, this paper presents a comprehensive overview of the design and simulation of heterostructures for optoelectronic devices using compound

semiconductors. We delve into the fundamental principles governing the electronic band structure, carrier transport mechanisms, and optical gain characteristics of heterostructures, highlighting the latest advancements and challenges in this rapidly evolving field. Through a detailed examination of the design considerations and simulation methodologies, we aim to provide valuable insights into the development of next-generation optoelectronic devices with enhanced performance and functionality.

II. DESIGN SPECIFICATIONS AND STRUCTURAL INFORMATION

In this study, we focus on designing and modeling a nanoscale structure composed of layers of materials InGaAs/GaAsSb to analyze the computation of energy wave functions and optical gain. Understanding the lasing characteristics of the proposed heterostructure necessitates a thorough understanding of bulk materials, which serve as the foundation for studying nanoscale structures. Figures 1 and 2 depict the band structure diagrams of the ternary materials InGaAs and GaAsSb, respectively, at room temperature (300 K). The valence band of these materials comprises three bands: the heavy-hole band (HHB), the light-hole band (LHB), and the split-off sub-band (SOB), distinguished based on their effective mass.

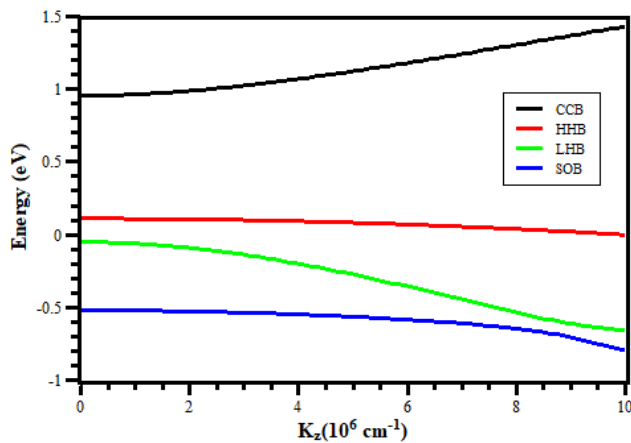


Fig.1. Band constructions of ternary compound InGaAs / GaAs

The heavy hole sub-band exhibits a higher effective mass compared to the light hole sub-band, while the light hole bands demonstrate a steeper energy slope than the heavy hole bands. The split-off band, positioned considerably below the conduction band, holds minimal significance due to its negligible energy. A prevalent challenge in semiconductor lasers lies in the elevated effective mass of the valence band. This issue is particularly common in group III-V semiconductors, stemming from a notable

imbalance in the effective masses of charge carriers between the valence and conduction bands.

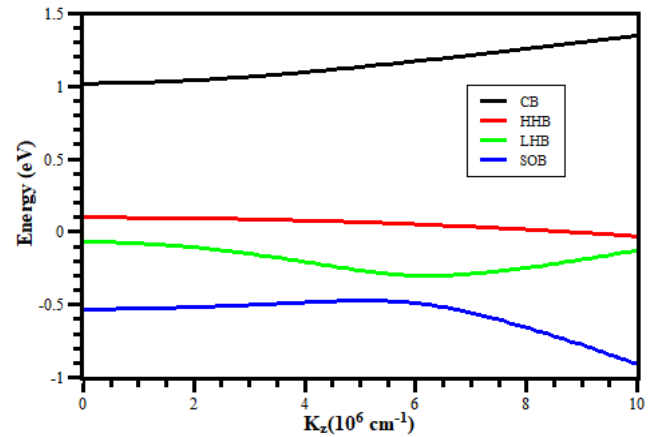


Fig. 2. Band constructions of ternary compound GaAsSb₀ /GaAs

The focal structure under examination comprises a p-type InGaAs layer sandwiched between n-type layers of GaAsSb material. With its symmetric energy bandgap, the InGaAs material functions as a quantum well, while the GaAsSb material serves as the barrier layer for charge carriers. The quantum well layer (InGaAs) measures 2 nm in width, while the barrier layer (GaAsSb) spans 4 nm. The entire structure is analyzed on a GaAs substrate at room temperature (300 K). Figure 3 illustrates the energy band diagram for the designed heterostructure.

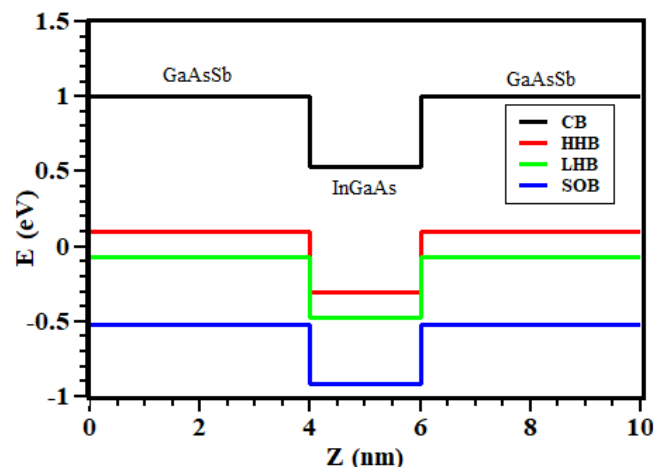


Fig. 3. Energy band diagram of the designed heterostructure

In the process of designing heterostructures tailored for specific applications, the selection of materials and the thickness of layers are pivotal factors influencing the emitted wavelength or radiated energy at the nanoscale level. In this study, the width or thickness of layers (denoted as Z) is meticulously determined through multiple calculations to optimize carrier confinement and effective

recombination of charge carriers. This optimization strategy aims to enhance optical gain at the desired 1550 nm wavelength.

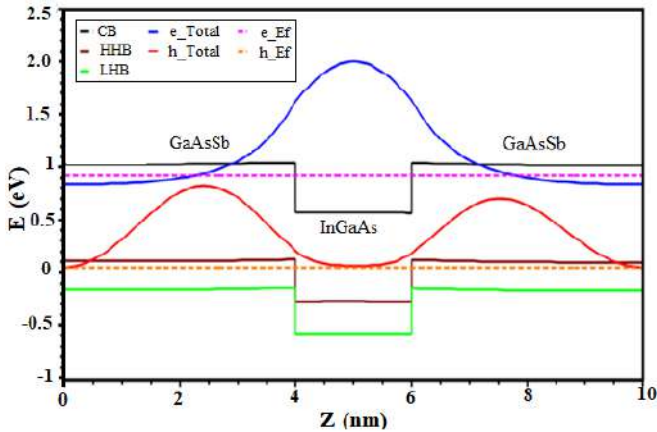


Fig 4. The energy wave function of the designed heterostructure

Analysis of energy wavefunction and band dispersion

The primary objective of this study is to develop a nanoscale heterostructure capable of emitting radiation at a wavelength of 1550 nm with a high optical gain, crucial for

Table 1. Compound semiconductor key material parameters at 0 K [12]

Material	Lattice Constant (A)	Band Gap (eV)	Effective mass(m_e/m_0)	γ_1	γ_2	γ_3
GaAs	5.653	1.51	0.067	6.98	2.06	2.93
InAs	6.058	0.41	0.026	20	8.5	9.2
AlAs	5.661	3.09	0.15	3.76	0.82	1.42
AlSb	6.135	2.38	0.14	5.18	1.19	1.97
GaSb	6.095	0.81	0.039	13.4	4.7	6

Analysis of optical gain characteristics

To evaluate the performance of the designed heterostructure in terms of amplification, the optical gain is calculated. Figure 5 illustrates the behavior of the computed optical gain with respect to emitted energy. At a temperature of 300 K, the designed heterostructure demonstrates an optical gain of approximately 6000/cm at a radiation energy of 0.8 eV. This energy corresponds to a wavelength of 1550 nm when converted from energy to wavelength. Consequently, the analyzed results affirm that the proposed design yields a higher optical gain compared to recently designed heterostructures.

enhancing output power. Calculating optical gain necessitates understanding carrier confinement and their distributions. To ascertain carrier localizations, electronic wavefunctions for conduction band electrons and valence band holes are computed. Figure 4 illustrates the calculated wavefunctions for electrons (e_{total}) and holes (h_{total}), along with the electron Fermi energy levels.

In determining the confinement of charge carriers within the barrier and well regions, a 6×6 Luttinger-Kohn Hamiltonian with effective mass approximation has been employed. This Hamiltonian accounts for the six-band energy levels of split-off, light, and heavy hole bands, including spin up and down states. Figure 4 elucidates that electrons are predominantly confined within the quantum well material, while holes are confined within the barrier material. Consequently, there is an increase in electron density within the well region, resulting in heightened charge carrier recombination and greater optical gain. Table 1 outlines key parameters of compound semiconductors utilized in this study, including constants γ_1 , γ_2 , and γ_3 , which are Luttinger parameters associated with the effective mass of valence subbands.

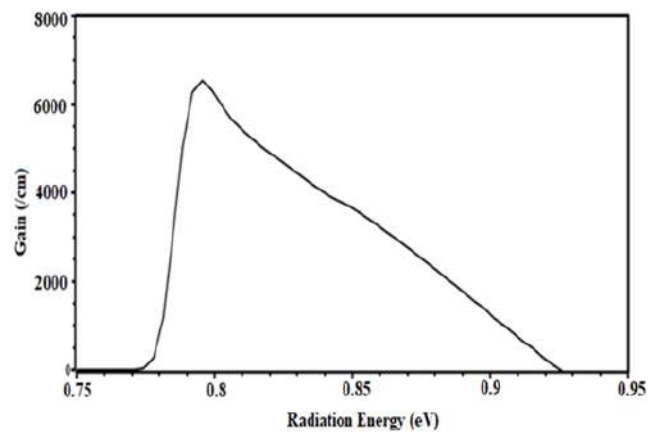


Fig 5: Optical gain characteristics of designed heterostructure

III. RESULTS AND CONCLUSION

this research presents a comprehensive investigation into the design and performance evaluation of a nanoscale heterostructure aimed at emitting radiation with a wavelength of 1550 nm and achieving high optical gain. Through meticulous calculations and analysis, the study demonstrates that the designed heterostructure, consisting of ternary compound materials, exhibits promising characteristics for optoelectronic applications. By employing a 6×6 Luttinger-Kohn Hamiltonian and considering carrier confinement, the study reveals favorable carrier distributions, particularly with electrons confined in the quantum well material and holes within the barrier material. This confinement leads to increased carrier recombination and enhanced optical gain, as validated by the calculated energy dispersion profile and optical gain behavior.

IV. REFERENCES

- [1] P.A. Alvi, "Strain-induced non-linear optical properties of straddling-type indium gallium aluminum arsenic/indium phosphide nanoscale-heterostructures", *Material Science in Semiconductor Processing*, Elsevier, Vol.-31, no.-10, pp.106–115, March 2015.
- [2] P.A. Alvi, Pyare Lal, S. Dalela, M.J. Siddiqui, "An extensive study on simple and GRIN SCH-based $\text{In}_{0.71}\text{Ga}_{0.21}\text{Al}_{0.08}\text{As}/\text{InP}$ lasing heterostructures", *Physica Scripta*, Vol.- 85, no.-3, pp. 035402(1)- 035402(9), 2012.
- [3] Baile Chen, A.L. Holmes Jr, "Modelling of the type-II $\text{InGaAs}/\text{GaAsSb}$ quantum well designs for mid infrared laser diodes by k.p. method", *SPIE Laser Technology for Defense and Security VIII*, Vol.- 8381, no.- 23, pp. F 1- F 7, 2012.
- [4] T. Yamamoto, K. Takada, M. Matsuda, S. Okumura, S. Akiyama, and M. Ekawa, "1.55 μm -Wavelength AlGaInAs Multiple-Quantum-Well Semi-Insulating Buried-Heterostructure Lasers", *IEEE 20th International Semiconductor Laser Conference*, 2006, Conference Digest, pp. 15-16,2006.
- [5] Md. Tanvir Hasan, Md. Azim Ullah, Md. Asaduzzaman, Ashraful G. Bhuiyan, "1.55 μm Laser Using InN -Based Quantum Well Heterostructure", *IEEE 5th International Conference on Electrical and Computer Engineering*, pp. 946-948,2008.
- [6] Vibha Kumari, Ashish, Swati Jha, Amit Rathi, , H. K. Nirmal, P. A. Alvi, "Optical Gain of InGaAlAs Quantum well with Different Barriers, Claddings and Substrates", *Journal of Optoelectronics Engineering, Science and Education Publishing*, Vol. 2, No. 2, pp. 42-45, 2014.
- [7] C. H. Pan, C. P. Lee, Design and modeling of InP -based $\text{InGaAs}/\text{GaAsSb}$ type-II "W" type quantum wells for mid-Infrared laser applications", *Journal of Applied Physics* 113, 043112, 2013.
- [8] Baile Chen, "Optical gain analysis of GaAs -based $\text{InGaAs}/\text{GaAsSbBi}$ type-II quantum wells lasers", *Optics Express* Vol. 25, Issue 21, pp. 25183-25192, 2017.
- [9] AM Khan, M Sharma, MI Khan, S Kattayat, G Bhardwaj, M Abu-Samak M, SH Saeed, PA Alvi, Optical Gain Characteristics of a Novel $\text{InAlAs}/\text{InGaAs}/\text{GaAsSb}$ Type-II Nano- Heterostructure, *Optik*, Volume 183, April 2019, Pages 842-848, 2019.
- [10] J. M. Luttinger, W. Kohn, "Motion of Electrons and Holes in Perturbed Periodic Fields". *Physical Review*. 97: 869. doi/10.1103/PhysRev.97.869, 1955
- [11] E. Yablonovitch and E. O.Kane, "Band Structure Engineering of Semiconductor Lasers for Optical Communications," *Journal of Light wave Technology*, Vol.- 6, no.- 8, pp. 1292-1299, August 1988.
- [12] I. Vurgafman, J.R. Meyer, L.R. Ram-Mohan, Band parameters for III-V compound semiconductors and their alloys, *J. Appl. Phys.* 89 (11), 5815-5875, 2001.

Fe₃O₄.CeO₂/SiO₂ oxide nanocomposite as a Fenton-like catalyst for degradation of Congo red

Nguyen Manh Ha¹, Bui Thi Hai Yen¹, Vu Ngoc Hai¹, Tran Ngoc Hieu¹, Nguyen Thi Phuong^{2*}

¹Faculty of Chemical Technology, Hanoi University of Industry, 298 Cau Dien, Bac Tu Liem, Hanoi, Vietnam

²Institute of Chemistry and Materials, 17 Hoang Sam, Nghia Do, Cau Giay, Hanoi, Viet Nam

*Email: nguyenphuongmta95@gmail.com

Received: 27 Feb 2024,

Receive in revised form: 10 Apr 2024,

Accepted: 19 Apr 2024,

Available online: 28 Apr 2024

©2024 The Author(s). Published by AI
Publication. This is an open access article under
the CC BY license

(<https://creativecommons.org/licenses/by/4.0/>)

Keywords— nanocomposite, Fenton-like
catalyst, degradation, oxidation catalysis,
Congo red.

Abstract— Congo red (CR) was broken down by a heterogeneous Fenton oxidation process using a catalyst that concurrently contained cerium dioxide and ferromagnetic oxide on a silicon dioxide substrate (Fe₃O₄.CeO₂/SiO₂). CeO₂ was prepared from Ce(NO₃)₃.6H₂O with a carrier SiO₂ generated from rice husks; Fe₃O₄ catalyst was prepared from FeCl₃.6H₂O and FeCl₂.4H₂O. X-ray diffraction (XRD), scanning electron microscopy (SEM-EDX), specific surface area (BET), and Fourier transform infrared (FTIR) spectroscopy were used to investigate the catalyst's characteristics. The oxidation of Congo red was used to measure the catalytic activity. Other factors examined included the amount of catalyst, the pH, the H₂O₂ ratio, and the decomposition duration.

I. INTRODUCTION

The textile dyeing industry is one of many traditional industries and has a long development history. According to statistics, the entire textile industry releases an average of about 70 million m³ of wastewater into the environment per year [1]. Typical pollutants are vital dyes, organic substances, or inorganic salts [2]. The Fenton system is considered the most effective in treating dyes, aromatic amines, etc. In particular, the heterogeneous Fenton reaction uses iron catalysts or combined iron catalysts on different support substrates. At the same time, other multivalent metals have been researched and developed strongly in recent years.

Cerium is a typical rare earth metal with a redox cycle between 3⁺ and 4⁺ oxidation states, providing high oxygen storage capacity [3]. Accordingly, Juan Liu et al. [3] reported that Fe₃O₄-CeO₂/activated carbon (AC) can remove ofloxacin and total organic carbon (TOC) with efficiencies of 95% and 54%, respectively. Aniruddha and colleagues [4] synthesized Fe₃O₄-CeO₂ that can help

decompose 89.2% of catechol in the catalytic system. SiO₂ material has long been known for many applications, such as catalytic materials, dielectric materials, gas adsorbents, heavy metal ion adsorbents, and inorganic carriers [5]. SiO₂ in amorphous form has inert properties, high durability, and a large specific surface area > 100 m²/g [6]. With these properties, SiO₂ helps increase the durability of catalytic materials and the efficiency of organic matter treatment, especially colored organic substances.

In this study, a catalyst containing combined Fe₃O₄ and CeO₂ carried on SiO₂ was synthesized and used for the Fenton process to decompose Congo Red dye. Influential factors for Congo red oxidation were studied, such as catalyst amount, H₂O₂ amount, pH, and time.

II. EXPERIMENTS

2.1. Chemical

FeCl₃.6H₂O ≥98.5%, FeCl₂.4H₂O ≥98.5%,
Ce(NO₃)₃.6H₂O ≥98%, HCl 36%, H₂O₂ 30%, HNO₃ 68%,

NH₃ 25%, Congo red (3,3'-([1,1'-biphenyl]-4,4'-diyl)bis(4-aminonaphthalene-1-sulfonic acid)) received from Macklin (China).

2.2. Preparation of SiO₂ from rice husk

SiO₂ is prepared from rice husk using the sol-gel method according to the following process [7]:

The rice husk is collected, washed with water, and allowed to dry naturally. Rice husks continue to be pretreated with a precisely measured 1 M HCl solution for a scientifically determined 2 hours at a controlled temperature of 105 °C. They are then washed with HCl acid and dried at 105 °C for 4 hours. The calcination process is carried out in an air environment at a scientifically determined temperature of 600 °C to altogether remove organic compounds. The ivory-white solid obtained after calcination is called rice husk ash, a scientifically proven precursor for SiO₂ preparation.

Weigh 10 g of rice husk ash into a 250 ml flask. Add 200 ml of 1 M NaOH solution and heat the mixture to 110 °C for 2 hours. At the end of the reaction, the mixture was allowed to cool to room temperature, the residue was removed, and the remaining liquid was collected. Add 200 ml of distilled water to the rice husk ash extract and stir well under stable temperature conditions of 30 °C. Adjust the solution pH to pH = 6 with 1M HCl to form a gel. The gel was aged 24 hours and washed with water until all Cl⁻ ions were gone. The gel was dried at 60 °C for 24 hours and calcined at 600 °C for 5 hours in an ambient atmosphere. The resulting SiO₂ is white and porous at the end of the process.

2.3. Preparation of Fe₃O₄.CeO₂/SiO₂ catalyst

Fe₃O₄.CeO₂/SiO₂ catalyst is prepared by co-precipitation method as follows:

Dissolve 0.6487g of FeCl₃.6H₂O in 20 mL of distilled water with 2 mL of 36% HCl solution (solution A). Do the same with 0.2386g FeCl₂.4H₂O (solution B). Continue to dissolve 0.6210g of Ce(NO₃)₃.6H₂O and 1 mL of 68% HNO₃ solution in 20 mL of distilled water (solution C).

4g of SiO₂ derived from rice husks was evenly dispersed in 150 mL of distilled water. The prepared solutions A, B, and C were added to the SiO₂ suspension under circular stirring for 30 minutes. Next, 2 M NH₃ solution was added to the suspension until the pH reached ~ 7. The mixture continued to be stirred for 60 minutes and filtered to collect the residue. The solid was washed with distilled water several times (3 to 5 times) and dried at 105 °C for 24 hours. Finally, the solid was calcined at 400 °C for 5 hours and reddish brown Fe₃O₄.CeO₂/SiO₂ was obtained.

2.4. Characterization of materials

The phase structure of the sample was examined by X-ray diffraction (XRD PANalytical X' Pert Powder, Netherlands) using Cu K α radiation. The scanning electron microscope characterized the microstructure and morphology (SEM HITACHI S-4800). The chemical states and compositions of the sample were performed by energy dispersive X-ray spectroscopy with mapping (EDX, HITACHI S-4800). The Brunauer–Emmett–Teller (BET) specific surface area and porosity of the samples were determined by nitrogen adsorption-desorption (NOVATouch LX2, QUANTACHROME, USA) at 77 K. Thermal gravimetric analysis (TGA/DTG NETZSCH STA 409 PC/PG, Germani) investigated the sample's thermodynamic property.

2.5. Congo Red catalytic oxidation

The Fenton oxidation of CR in solution by the Fe₃O₄.CeO₂/SiO₂ catalyst is meticulously conducted at room temperature. The substances are carefully placed into a 250 mL glass beaker containing 100mL of CR solution with a concentration of 100mg/L. The reaction time is precisely measured from the moment of H₂O₂ addition. We thoroughly investigate influential factors, including: Catalyst amount 0.05-0.25 g/100mL; pH 2-10; the volume of H₂O₂ (30%) 0.5-2.5/100 (V/V); Processing time is performed to determine the appropriate conditions for CR decomposition, samples are taken at 5-180 minute intervals then the optical density of the solution is measured on a G10S UV-Vis Spectrophotometer.

Efficiency (H %) of CR decomposition according to the formula:

$$H(\%) = \frac{C_0 - C_t}{C_0} \times 100\%$$

C₀ and C_t are the initial and remaining CR concentrations after time t (mg/L), respectively.

III. RESULT AND DISCUSSION

3.1. Characteristics of Cu-BTC

The results of the XRD spectrum of SiO₂ and the catalyst sample are presented in Fig. 1a. The results show that the XRD pattern of SiO₂ has only one diffraction peak with a reasonably broad base at about 23-26 ° and no cristobalite or tridymite crystalline phase peak. Thus, SiO₂ has the structure of amorphous silica material. In addition, on the XRD chart of the catalyst, peaks appear at positions corresponding to the scanning angle 2 θ including 30.2, 35.6, 57.1, and 62.8°, characterizing the existence of Fe₃O₄, similar to the study of Guaqiang Gan and colleagues [8]. Peaks at 28.6, 33.1, 47.5, and 56.4°, which are characteristic of CeO₂, were also obtained on the diffraction pattern and are consistent with the research of Keyan Li and colleagues

[9]. The existence of Fe_3O_4 and CeO_2 on SiO_2 has been confirmed through these results.

The FTIR spectrum (Fig. 1b) shows a peak at 544 cm^{-1} assigned to the stretching vibration of Fe-O in Fe_3O_4 . The appearance of a leading band in the region below 500 cm^{-1} is indicated for the stretching vibrations of Ce-O, similar to the study of D. Channei and colleagues [10]. The presence of SiO_2 is observed through two characteristic bands of the Si-O-Si bond (1086 and 795 cm^{-1}) and of Si-OH (984 cm^{-1}) [11].

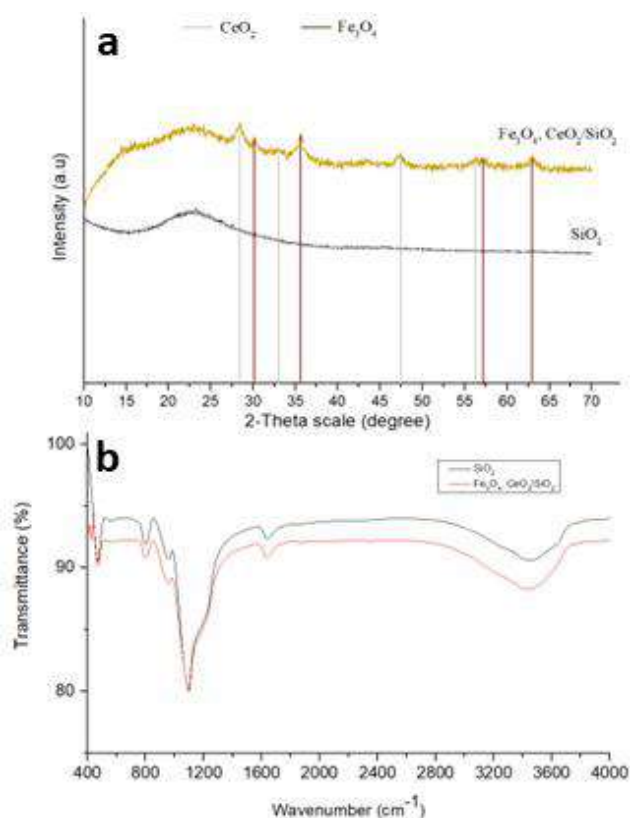


Fig. 1: XRD patterns (a) and FTIR spectrum (b) of SiO_2 and prepared $\text{Fe}_3\text{O}_4, \text{CeO}_2/\text{SiO}_2$

From Fig. 2a,b, $\text{Fe}_3\text{O}_4, \text{CeO}_2/\text{SiO}_2$ catalyst is spherical particles clustered together, with a uniform particle size $<250\text{ nm}$ and an average size of 150 nm . The EDX diagram with the elemental composition of the $\text{Fe}_3\text{O}_4, \text{CeO}_2/\text{SiO}_2$ catalyst is shown in Figure 2c. The catalyst was mainly silicon, ferromagnetic, and cesium oxides mixture. The Fe content is about 7.48% by mass (corresponding to 2.84% of the element). Meanwhile, the Ce content is about 5.71% by mass (corresponding to 0.86% element). The remaining SiO_2 accounts for 32.88% of the mass (corresponding to 24.33% of the component). Analysis results also show that the material is free of other impurities.

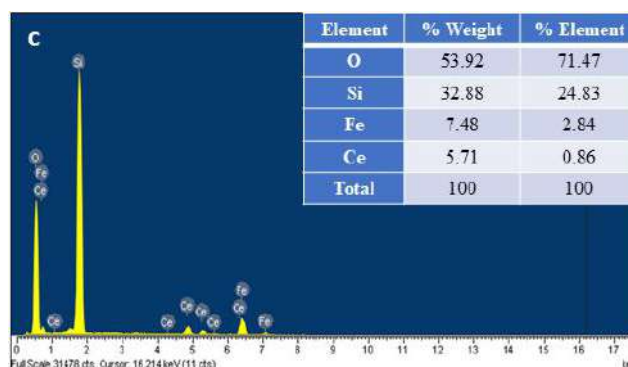
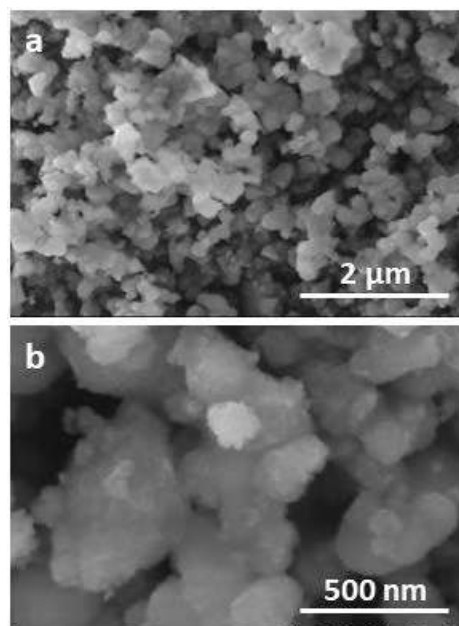


Fig. 2: SEM images (a, b) and EDX spectra (c) of SiO_2 and prepared $\text{Fe}_3\text{O}_4, \text{CeO}_2/\text{SiO}_2$.

Surface characteristics of the SiO_2 substrate (Figure 3a) show that it is a porous material with a specific surface area of $368.615\text{ m}^2/\text{g}$ and a large pore volume from $0.291 - 0.334\text{ cm}^3/\text{g}$. Therefore, adding metal oxides Fe_3O_4 and CeO_2 to SiO_2 does not change the material's pore structure and capillary size (Figure 3b). The pore volume value of the catalyst ranges from $0.276 - 0.317\text{ cm}^3/\text{g}$. However, the specific surface area of the catalyst decreased compared to the SiO_2 support from $368.615\text{ m}^2/\text{g}$ of SiO_2 to $299.68\text{ m}^2/\text{g}$ of the catalyst. The reason may be that Fe_3O_4 and CeO_2 particles, when placed on the SiO_2 substrate, will displace some of the SiO_2 pores, leading to a decrease in the specific surface area of the catalyst. The isothermal adsorption-desorption diagram of SiO_2 and catalyst (Figure 2a) shows that a hysteresis loop appears at the relative pressure range p/p_0 from 0.4 to 1.0 and is characteristic of medium capillary material. The pore sizes of SiO_2 and the catalyst are $3,505-4,208\text{ nm}$ and $4,216 - 4,642\text{ nm}$, respectively.

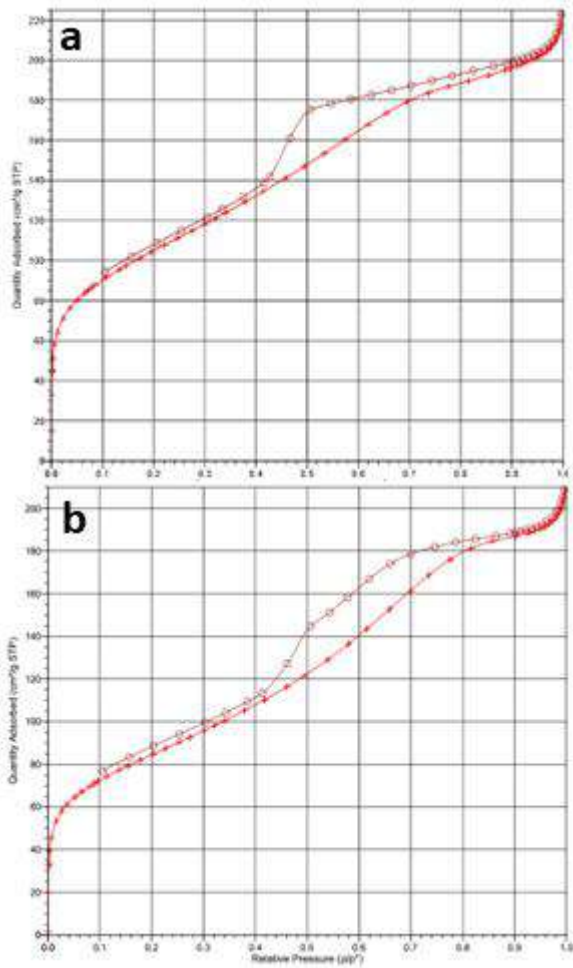


Fig .2: BET diagram of SiO₂ (a) and prepared Fe₃O₄.CeO₂/SiO₂ (b).

3.2. Congo Red catalytic oxidation

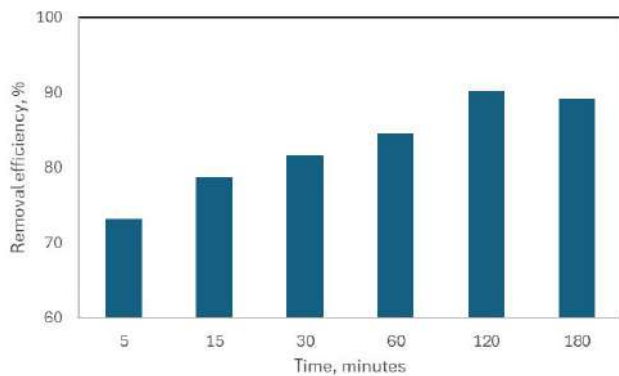


Fig .2: The effect of time on Congo red removal efficiency with Fe₃O₄.CeO₂/SiO₂.

Figure 3 presents the effect of time on Congo red removal efficiency of Fe₃O₄.CeO₂/SiO₂. The process efficiency increased rapidly from about 73.19% after 5 minutes to about 90.22% after 120 minutes of reaction. At this time, the Congo red catalytic oxidation process

occurred almost wholly. Thus, under the conditions and scope of the survey, the appropriate reaction time was 120 minutes.

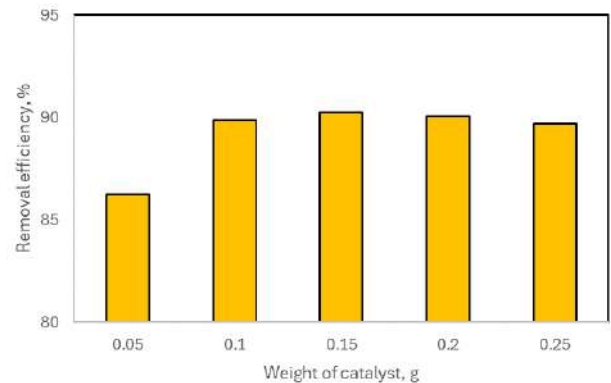


Fig .3: The effect of catalyst's weight on Congo red removal efficiency with Fe₃O₄.CeO₂/SiO₂.

The results of the influence of the amount of Fe₃O₄.CeO₂/SiO₂ catalysts are shown in Figure 3. The results show that increasing the amount of catalyst increases Congo red treatment efficiency, as demonstrated by the practical value. The H% yield increased and reached the highest catalytic ratio at 0.15 g/100 mL, reaching 90.22 %. However, when adding a catalyst, the processing efficiency does not increase. A slight decrease to 90.04 % corresponds to a catalyst amount of 0.2 g/100 mL. The cause may be due to the reaction of *HO and Fe²⁺ produced during the reaction [12]. From there, the most appropriate catalyst content ratio is 0.15 g/100 mL.

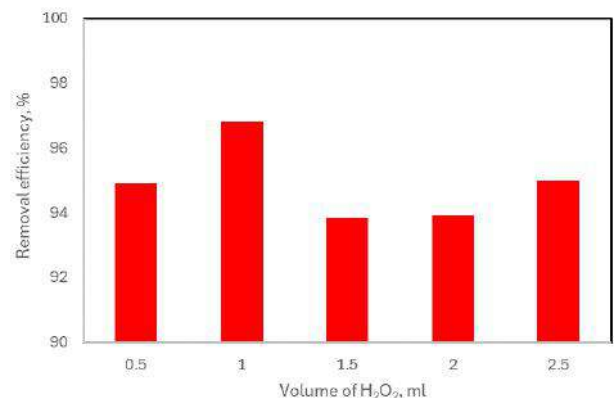
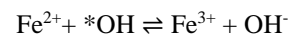
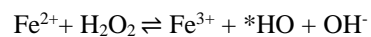
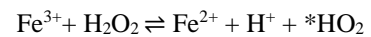


Fig .4: The effect of H₂O₂'s volume on Congo red removal efficiency with Fe₃O₄.CeO₂/SiO₂.

The results of studying the influence of H₂O₂ amount on Congo red oxidation efficiency are shown in Figure 4. The

results show that when the proportion of H_2O_2 (30%) increases, the decomposition efficiency increases. Specifically, when the H_2O_2 ratio is 0.5 mL/100 mL at 120 min, and the amount of catalyst added is 0.15g, the Congo red treatment efficiency reaches about 94.90%. Then, it increased and reached the highest efficiency of 96.79% at the ratio of 1 mL/100 mL. The reason is that an increase in H_2O_2 concentration leads to an increase in $\cdot\text{OH}$ free radicals and increases the efficiency of the Congo red decomposition process [13]. However, when the amount of H_2O_2 is in excess, it will create $\cdot\text{OOH}$ radical according to the reaction:



The oxidation property of $\cdot\text{OOH}$ radical is weaker than that of $\cdot\text{OH}$ radical, leading to a slight decrease in Congo red oxidation efficiency. Thus, the appropriate H_2O_2 ratio is 1 mL/100 mL.

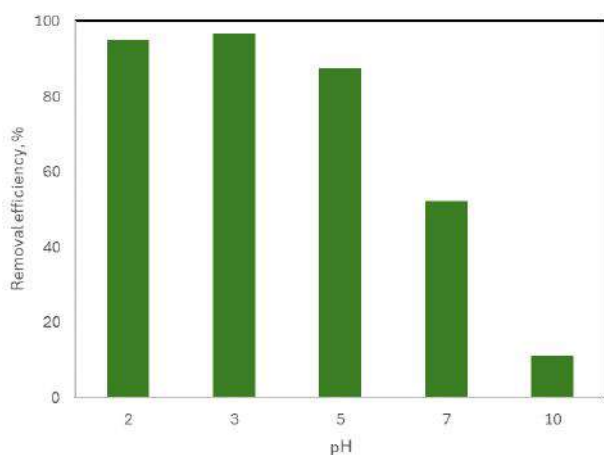


Fig. 6: The effect of pH on Congo red removal efficiency with $\text{Fe}_3\text{O}_4.\text{CeO}_2/\text{SiO}_2$.

The results of studying the influence of pH on the Congo red decomposition process are presented in Figure 6. The results show that at pH range 2-3, the Congo red decomposition efficiency has a stable value of 95 ~ 97% and reaches the highest efficiency at pH = 3. However, at pH > 3, Congo red decomposition efficiency drops sharply. In an acidic environment, the catalytic reaction with H_2O_2 creates high oxidation properties, and hydroxyl radicals have the effect of quickly decomposing organic pollutants [4]. Therefore, the pH value chosen is 3.

IV. CONCLUSION

The materials $\text{Fe}_3\text{O}_4.\text{CeO}_2/\text{SiO}_2$ was synthesized by the co-precipitation method from $\text{FeCl}_3.6\text{H}_2\text{O}$, $\text{FeCl}_2.4\text{H}_2\text{O}$, $\text{Ce}(\text{NO}_3)_3.6\text{H}_2\text{O}$ with atomic ratio 5%Fe: 4%Ce on support of SiO_2 (from rice husk ash). The specific surface area of the material reaches $299.68 \text{ m}^2/\text{g}$, with an average pore size.

The material was used as a catalyst for the Fenton process to degrade Congo red with appropriate conditions: catalyst amount 0.15g/100ml Congo red solution; pH = 3; volume ratio H_2O_2 30%/100ml Congo red solution = 1mL; Decomposition time was 120 minutes with efficiency reaching 96.79%.

ACKNOWLEDGEMENTS

This research is funded by the Faculty of Chemical Technology, Hanoi University of Industry.

REFERENCES

- [1] Pham Van Liem, "Prioritize the development of clean technology in Vietnam's textile and dyeing industry", Industry and Trade Magazine, 2020.
- [2] Dang Thi Thom, Nguyen Thanh Duong, Nguyen Chi Thanh, Tran Manh Hai, Do Van Manh, Nguyen Hoai Chau, Trinh Van Tuyen, "Research on the ozonation process to treat Methyl Orange dye in textile wastewater", Conference Proceedings: Basic Research in "Earth and Environmental Sciences" 2019.
- [3] Juan Liu, Xia Wu, Jingjing Liu, Conglu Zhang, Qi Hu, Xiaohong Hou, "Ofloxacin degradation by $\text{Fe}_3\text{O}_4\text{-CeO}_2/\text{AC}$ Fenton-like system: Optimization, kinetics, and degradation pathways", Molecular Catalysis 465 (2019) 61–67.
- [4] Aniruddha Gogoi, Madhukar Navgire, Kanak Chandra Sarma, Parikshit Gogoi, " $\text{Fe}_3\text{O}_4\text{-CeO}_2$ metal oxide nanocomposite as a Fenton-Like heterogeneous catalyst for degradation of catechol", Chemical Engineering Journal (2016).
- [5] J. F. Chen, H. M. Ding, J. X. Wang, L. Shao, "Preparation and characterization of porous hollow silica nanoparticles for drug delivery application", Biomaterials, 25(3), 723-727 (2003).
- [6] Nguyen Thi Ha Chi, Doan Trung Dung, Pham Ngoc Chuc, Duong Thi Lim, Dao Ngoc Nhiem, "Synthesis of nanometer-sized CeO_2 materials on SiO_2 substrate and study of their photocatalytic ability", Journal of Chemistry, 2018, 56(1),117-121.
- [7] Nguyen Manh Ha, Tran Thi Huong & Ninh The Son (2023), "Synthesis of the $\text{MnO}_2\text{-Fe}_3\text{O}_4$ catalyst support on amorphous silica: a new Fenton's reagent in the degradation of the reactive blue-19 in aqueous solution", Journal of Environmental Science and Health, Part A, 58:5, 506-514.
- [8] Keyan Li, Yongqin Zhao, Chunshan Song, Xinwen Guo, "Magnetic ordered mesoporous $\text{Fe}_3\text{O}_4/\text{CeO}_2$ composites with synergy of adsorption and Fenton catalysis", Applied Surface Science Volume 425, 15 December 2017, Pages 526-534.
- [9] Yang Wang, Haoran Sun, Tong Zhang, Yuhua Shen, Jian Zhang, Jialing Xia; "Synthesis and Property of Multifunctional $\text{Fe}_3\text{O}_4@/\text{SiO}_2@/\text{CeO}_2@/\text{Au}$ Composite Microspheres", Brief Reports and Reviews Vol. 7, No. 6 (2012) 1250042.
- [10] D. Channei, B. Inceesungvorn, N. Wetchakun, and S. Phanichphant, "Synthesis of $\text{Fe}_3\text{O}_4/\text{SiO}_2/\text{CeO}_2$ Core-Shell

- Magnetic and Their Application as Photocatalyst”, *Journal of Nanoscience and Nanotechnology*, Vol. 14, 7756–7762, 2014.
- [11] Guoqiang Gan, Juan Liu, Zhixi Zhu, Ziran Yang, Conglu Zhang, Xiaohong Hou; “A novel magnetic nanoscaled $\text{Fe}_3\text{O}_4/\text{CeO}_2$ composite prepared by oxidation-precipitation process and its application for degradation of orange G in aqueous solution as Fenton-like heterogeneous catalyst”; *Chemosphere*, 168(2017), 254–263.
- [12] Lejin Xu, Jianlong Wang; “Magnetic Nanoscaled $\text{Fe}_3\text{O}_4/\text{CeO}_2$ Composite as an Efficient Fenton-Like Heterogeneous Catalyst for Degradation of 4-Chlorophenol”; *Environ. Sci. Technol.* 2012, 46, 18, 10145–10153.
- [13] Lejin Xu, Jianlong Wang, “Degradation of 2,4,6-trichlorophenol using magnetic nanoscaled $\text{Fe}_3\text{O}_4/\text{CeO}_2$ composite as a heterogeneous Fenton-like catalyst”, *Separation and Purification Technology* Volume 149, 27 July 2015, Pages 255-264.